
Differentiable Gaussianization Layers for Inverse Problems Regularized by Deep Generative Models

Dongzhuo Li

ExxonMobil Technology & Engineering Company
dongzhuo.li@exxonmobil.com

Abstract

Deep generative models such as GANs and normalizing flows are powerful priors. They can regularize inverse problems to reduce ill-posedness and attain high-quality results. However, the latent vector of such deep generative models can fall out of the desired high-dimensional standard Gaussian distribution during an inversion, particularly in the presence of noise in data or inaccurate forward models. In such a case, deep generative models are ineffective in attaining high-fidelity solutions. To address this issue, we propose to reparameterize and Gaussianize the latent vector using novel differentiable data-dependent layers wherein custom operators are defined by solving optimization problems. These proposed layers constrain an inversion to find feasible in-distribution solutions. We tested and validated our technique on three inversion tasks: compressive-sensing MRI, image deblurring, and eikonal tomography (a nonlinear PDE-constrained inverse problem), using two representative deep generative models: StyleGAN2 and Glow, and achieved state-of-the-art results.

1 Introduction

Inverse problems are ubiquitous and crucial to solve in scientific endeavors and our daily life. For example, astrophysicists use radio electromagnetic data to image galaxies and black holes [19, 1]. Geoscientists use seismic recordings to reveal the internal structures of Earth [61, 62, 64]. Biomedical engineers and doctors use X-ray projections, ultrasound measurements, and magnetic resonance data to reconstruct images of human tissues and organs [37, 15, 45].

Formally, we write the forward mapping as

$$\mathbf{d} = f(\mathbf{m}) + \epsilon, \quad (1)$$

where f stands for a forward model that usually describes some physical process, ϵ denotes noise, \mathbf{d} the observed data, and \mathbf{m} the parameters to be estimated. The forward model can be either linear or nonlinear and either explicit or implicitly defined by solving partial differential equations (PDEs). This study considers three representative inverse problems: **Compressive Sensing MRI**, **Deblurring**, and **Eikonal (traveltime) Tomography**, which have important applications in medical science, geoscience, and astronomy. The details of each problem and its forward model are in appendix A.

The forward problem maps \mathbf{m} to \mathbf{d} , while the inverse problem estimates \mathbf{m} given \mathbf{d} . Unfortunately, inverse problems are generally under-determined with infinitely many compatible solutions and intrinsically ill-posed because of the nature of the physical system. Worse still, the observed data are usually noisy, and the assumed forward model might be inaccurate, exacerbating the severeness of ill-posedness. These challenges require using regularization to inject *a priori* knowledge into inversion processes to obtain plausible and high-fidelity results. Therefore, an inverse problem is

usually posed as an optimization problem:

$$\arg \min_{\mathbf{m}} (1/2) \|\mathbf{d} - f(\mathbf{m})\|_2^2 + \mathcal{R}(\mathbf{m}), \quad (2)$$

where $\mathcal{R}(\mathbf{m})$ is the regularization term. Beyond traditional regularization methods such as the Tikhonov regularization and Total Variation (TV) regularization, deep generative models (DGM), such as VAEs [33], GANs [17], and normalizing flows [13, 14, 32, 53, 47], have shown great potential in regularizing inverse problems [7, 63, 18, 52, 3, 48, 38, 56, 67]. Such deep generative models directly learn from training data distributions and are a powerful and versatile prior. They map latent vectors to outputs distributed according to an *a priori* distribution: $\mathbf{m} = g(\mathbf{z}) \sim p_{\text{target}}, \mathbf{z} \sim \mathcal{N}(\mathbf{0}, \mathbf{I})$, for example. The framework of DGM-regularized inversion [7] is

$$\arg \min_{\mathbf{z}} (1/2) \|\mathbf{d} - f \circ g(\mathbf{z})\|_2^2 + \mathcal{R}'(\mathbf{z}), \quad (3)$$

where the deep generative model g reparameterizes the original variable \mathbf{m} , acting as a hard constraint. Instead of optimizing for \mathbf{m} , we now estimate the latent variable \mathbf{z} and retrieve the inverted \mathbf{m} by forward mappings. Since the latent distribution is usually a standard Gaussian, the new (optional) regularization term $\mathcal{R}'(\mathbf{z})$ can be chosen as $\beta \|\mathbf{z}\|_2^2$ for GANs and VAEs, where β is a weighting factor. See Appendix J.1 for more details on a similar formulation for normalizing flows. Since the optimal β depends on the problem and data, tuning β is highly subjective and costly.

However, this formulation of DGM-regularized inversion still leads to unsatisfactory results if the data are noisy or the forward model is inaccurate, as shown in Fig. 1, even if we fine-tune the weighting parameter β .

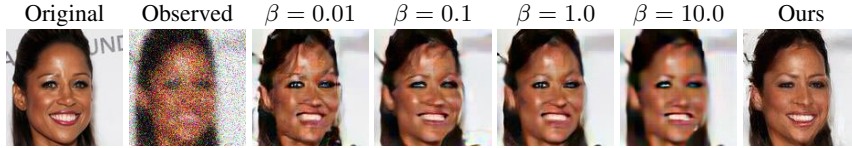


Figure 1: Glow-regularized deblurring results with different weighting factor β s and our Gaussianization layers.

This phenomenon is caused by the deviation of the latent vector from a typical sample from a standard Gaussian distribution. The generator may map out-of-distribution latent vectors to unrealistic results.

In this paper, we propose a set of differentiable Gaussianization layers to reparameterize and Gaussianize the latent vectors of deep generative models for inverse problems. We test and compare our technique with competing methods on three inversion tasks: compressive-sensing MRI, image deblurring, and eikonal tomography (a nonlinear PDE-constrained inverse problem), using two representative deep generative models: StyleGAN2 [27] and Glow [31].

2 Method

2.1 Overview - reparameterization with Gaussianization layers

Our proposed solution is to reparameterize the latent space vector \mathbf{z} by another random vector \mathbf{v} using differentiable Gaussianization layers, which defines a mapping h . With this new parameterization, even if the optimization pushes \mathbf{v} out of the Gaussian distribution, the mapping h can shape it towards a typical example from the desired high-dimensional standard Gaussian distribution: $\mathbf{z} = h(\mathbf{v}), \mathbf{v} \in \mathbb{R}^n$, s.t. $\mathbf{z} \sim \mathcal{N}(\mathbf{0}, \mathbf{I})$. Therefore, the original DGM-regularized inversion 3 becomes

$$\arg \min_{\mathbf{v}} (1/2) \|\mathbf{d} - f \circ g \circ h(\mathbf{v})\|_2^2. \quad (4)$$

The Gaussianization layers keep the optimization problem unconstrained, enabling us to use highly efficient unconstrained optimizers, such as L-BFGS [50] and ADAM [30].

Similar to the whitening layers [20, 57], the Gaussianization layers work on latent vector patches. We extract non-overlapping patches from tensors in the multi-scale architectures of Glow and StyleGAN2

(Appendix C). For Glow, we propose two patch-extraction/reparameterization schemes. For example, suppose that if a latent tensor at one scale has a shape of $n_c \times n_x \times n_y$, we partition it into non-overlapping patches of dimension $n_c \times w \times w$. We here assume that the patch tensors are independent and identically distributed (i.i.d.), *i.e.*, the vectorized patch tensors $\mathbf{v}_i \in \mathbb{R}^D$ ($D = n_c \times w \times w$, $i = 1, \dots, N$) are i.i.d. random vectors. This assumption is justified since patches far apart appear independent and that CNN filters are local operators. We will revisit this assumption in the upcoming Sec. 2.2 about the ICA layer.

If we concatenate latent patches into a long vector $\mathbf{v} = (\mathbf{v}_1^\top, \dots, \mathbf{v}_N^\top)^\top$, the Gaussianization mapping becomes $h = \text{diag}(h', \dots, h')$, where we need to construct the mapping $h' : \mathbf{v}_i \rightarrow \mathbf{z}_i$, such that $\mathbf{z}_i \sim \mathcal{N}(\mathbf{0}, \mathbf{I})$. As a result, the concatenation of $\mathbf{z}_i, i=1, \dots, N$ will also be a random vector distributed as a standard Gaussian. To construct h' , from the perspective of optimization, we minimize the KL-divergence $D_{\text{KL}}(\mathbf{z}_i \| \mathcal{N}(\mathbf{0}, \mathbf{I}))$, which can be decomposed as the sum of the multi-information $I(\mathbf{z}_i)$ and the marginal negentropy $J_m(\mathbf{z}_i)$ [10]:

$$D_{\text{KL}}(p(\mathbf{z}_i) \| \mathcal{N}(\mathbf{0}, \mathbf{I})) = I(\mathbf{z}_i) + J_m(\mathbf{z}_i), \quad (5)$$

where

$$I(\mathbf{z}_i) = D_{\text{KL}}\left(p(\mathbf{z}_i) \left\| \prod_j^D p_j(z_i^{(j)})\right.\right), \text{ and } J_m(\mathbf{z}_i) = \sum_{j=1}^D D_{\text{KL}}\left(p_j(z_i^{(j)}) \left\| \mathcal{N}(0, 1)\right.\right). \quad (6)$$

Here $z_i^{(j)}$ denotes the j -th component of patch vector \mathbf{z}_i , and p_j stands for the marginal PDF for that component. Taking advantage of the fact that the KL divergence and a standard Gaussian in Eq. 5 are invariant to an orthogonal transformation and that the multi-information term is invariant to a component-wise invertible transformation, we propose to conduct Gaussianization in the following steps, as the framework in [10, 36]:

1. Minimize the multi-information $I(\mathbf{z}_i)$ – making the components of patch vectors statistically independent. This is done by an orthogonal transformation that keeps the overall KL divergence the same but increases the negentropy $J_m(\mathbf{z}_i)$.

2. Minimize the marginal negentropy $J_m(\mathbf{z}_i)$ by component-wise operations that perform 1D Gaussianization of marginal distributions $p_j, j=1, \dots, D$. The multi-information does not change under component-wise invertible operations. Therefore, the overall KL divergence between \mathbf{z}_i and the Gaussian distribution decreases.

Unlike conventional neural network layers, the input-data-dependent layers are not defined by learning from a dataset ahead of time but by solving certain optimization problems on the job (Fig. 2). Special care should be taken to implement the gradient computation correctly and ensure that they pass the finite-difference convergence test (Appendix F). As an overview, the composition of our proposed layers is:

$\mathbf{v} \rightarrow \text{Whitening} \rightarrow \text{ICA} \rightarrow \text{Yeo-Johnson} \rightarrow \text{Lambert } W \times F_X \rightarrow \text{Standardization} \rightarrow \mathbf{z}$

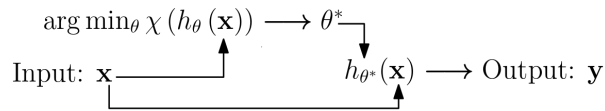


Figure 2: Illustration of the forward computation of optimization-based ICA, Yeo-Johnson, and Lambert $W \times F_X$ layers. The back-propagation of gradients is enabled by a trick in automatic differentiation detailed in Appendix F.

2.2 Reducing multi-information – ICA layer

The orthogonal matrix W is constructed by the independent component analysis (ICA). The input is the patch vectors $\{\mathbf{v}_i\}, i=1, \dots, N$ extracted from \mathbf{v} . The ICA algorithm first computes the input-dependent orthogonal matrix W and then computes $\mathbf{p}_i = W^\top \mathbf{v}_i, i=1, \dots, N$ as the output. The

orthogonal matrix \mathbf{W} makes the entries of each \mathbf{p}_i independent random variables. Therefore, the concatenated output random vector $\mathbf{p} = [\mathbf{p}_1, \mathbf{p}_2, \dots, \mathbf{p}_N]$ has independent components, based on the i.i.d. assumption about $\{\mathbf{v}_i\},_{i=1, \dots, N}$ mentioned in Sec. 2.1. The ICA layer also implicitly assumes that $\{\mathbf{v}_i\},_{i=1, \dots, N}$ are i.i.d. training examples. In practice, neighboring pixels from different patches may not be independent. Still, just like in the cocktail party problem, the performance of ICA does not depend strongly on the independent assumption as long as there are sufficient data [49].

We use the FastICA algorithm [21, 23], which employs a fixed-point algorithm to maximize a contrast function Φ (e.g., the logcosh function) for our ICA layer to reduce multi-information.

The FastICA algorithm typically requires that the data are pre-whitened. We adopt the ZCA whitening method or the iterative whitening method introduced in [21] (Appendix D). With the whitened data, we compute \mathbf{W} using a damped fixed-point iteration scheme:

$$\mathbf{W} = \frac{1}{N} \left[\alpha \mathbf{V} \phi(\mathbf{W}^\top \mathbf{V})^\top - \mathbf{W} \text{diag}(\phi'(\mathbf{W}^\top \mathbf{V}) \mathbf{1}) \right], \quad (7)$$

where $\mathbf{1}$ is an all-one vector, the column vectors of \mathbf{V} are $\{\mathbf{v}_i\},_{i=1, \dots, N}$, $\phi(\cdot) = \Phi'(\cdot)$, $\alpha \in (0, 1)$, and we use $\alpha = 0.8$ throughout our experiments. To save computation time, we only perform a maximum of 10 iterations. The details of the whole algorithm can be found in Appendix D.

We set the initial \mathbf{W} as an identity matrix. If the input vectors are already i.i.d. Gaussian (in-distribution), the computed \mathbf{W} will still be an identity matrix, which maps the input to the same output. In practice, the empirical distribution from finite samples is not a standard Gaussian, so \mathbf{W} is not an identity matrix but another orthogonal matrix, which still maps i.i.d. standard Gaussian input vectors to i.i.d. standard Gaussian vectors as output.

2.3 Reducing marginal negentropy

For 1D Gaussianization, we choose a combination of the Yeo-Johnson transformation that reduces skewness and the Lambert $W \times F_X$ transformation that reduces heavy-tailedness. Both are layers based on optimization problems with only one parameter, which is cheap to compute and is easy to back-propagate the gradient. Eq. 6 requires us to perform such 1D transformations for each component of the random vectors. In other words, we need to solve the same optimization problem for D times, which imposes a substantial computational burden. Instead, we empirically find it acceptable to share the same optimization-generated parameter across all components. In other words, we perform only a single 1D Gaussianization, treating all entry values in the latent vector as the data simultaneously.

Power transformation layer We propose to use the power transformation or Yeo-Johnson transformation [70] to reduce the skewness of distributions:

$$s(\lambda, p) = \begin{cases} \left((p+1)^\lambda - 1 \right) / \lambda, & p \geq 0, \lambda \neq 0, \\ \log(p+1), & p \geq 0, \lambda = 0, \\ -\frac{(-p+1)^{2-\lambda} - 1}{(2-\lambda)}, & p < 0, \lambda \neq 2, \\ -\log(-p+1), & p < 0, \lambda = 2, \end{cases} \quad (8)$$

where p is an input value, s is an output value, and λ is the parameter to be estimated. As shown in Fig. 3(a), the form of the Yeo-Johnson activation function depends on parameter λ . If $\lambda = 1$, the mapping is an identity mapping. If $\lambda \geq 1$, the activation function is convex, compressing the left tail and extending the right tail, reducing the left-skewness. If $\lambda \leq 1$, the activation function is concave, which oppositely reduces the right-skewness. The only parameter λ is determined by solving an optimization problem that minimizes the negentropy:

$$\lambda = \arg \max_{\lambda} l(\lambda|\mathbf{p}) = \arg \max_{\lambda} -\frac{n}{2} \log(\text{Var}(s(\lambda, p_i))) + (\lambda - 1) \sum_{i=1}^n \text{sign}(p_i) \log(|p_i| + 1), \quad (9)$$

where \mathbf{p} is the input data vector with entries $p_i,_{i=1, \dots, n}$. We refer the readers to Appendix D for details on implementation and algorithm.

Lambert $W \times F_X$ layer Due to noise and inaccurate forward models, we observe that the distribution of latent vector values tends to be shaped as a heavy-tailed distribution during the inversion process. To reduce the heavy-tailedness, we adopt the Lambert $W \times F_X$ method detailed in [16].

Let X be a random variable whose CDF is F_X , with mean μ_X and standard deviation σ_X . The following transformation with a heavy-tail parameter $\delta \geq 0$:

$$S = \left(U \exp\left(\frac{\delta}{2} U^2\right) \right) \sigma_X + \mu_X, \quad (10)$$

where $U = (X - \mu_X) / \sigma_X$, is a bijection and maps X to another random variable S with heavier tails.

We use the parameterized Lambert $W \times F_X$ distribution family to approximate a heavy-tailed input and solve an optimization to estimate an optimal δ (Appendix D), with which the inverse transformation maps the heavy-tailed distribution towards a Gaussian.

Fig. 3(b) shows that the Lambert $W \times F_X$ layer acts as a nonlinear squashing function. As δ increases, it compresses more the large values and reduces the heavy-tailedness. Intuitively, the Lambert $W \times F_X$ layer can also be interpreted as an intelligent way of imposing constraints on the range of values instead of a simple box constraint. We refer the readers to Appendix D for more details about the optimization problem and implementation.

Standardization with temperature Since the Lambert $W \times F_X$ layer output may not necessarily have a zero mean and a unit (or a prescribed) variance, we standardize the output using

$$z = (\mathbf{x} - \mathbb{E}[\mathbf{x}]) / \sqrt{\text{Var}(\mathbf{x})} * \gamma, \quad (11)$$

where γ is the temperature parameter suggested in [31].

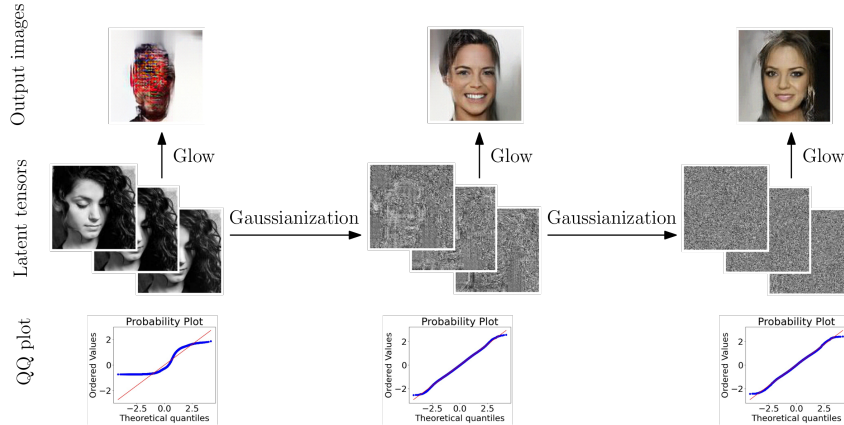


Figure 4: The effects of Gaussianization layers. As an exaggerated example, we use a standardized (with a temperature of 0.8) image as a latent tensor. The latent tensor components are not independent, and the values do not follow a Gaussian distribution as indicated by the QQ-plot. Then, we apply the proposed Gaussianization layers twice, which destroy the patterns and make the values approximately distributed as a Gaussian with a temperature of 0.8. We applied a rolling operation (Appendix J) before the second pass of Gaussianization. After only one pass, the image output using the normalizing flow becomes plausible. In fact, only one set of these layers is adequate for inversion.

In summary, we illustrate the effects of the Gaussianization layers in Fig. 4, which shows that these layers eliminate latent space patterns, *i.e.*, making latent pixels independent, and shape their value distribution towards an isotropic Gaussian distribution (with a given temperature).

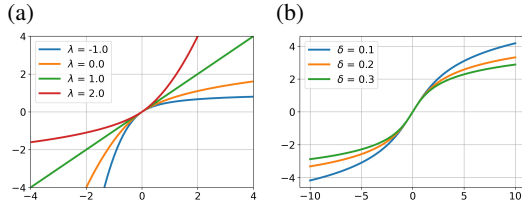


Figure 3: The nonlinear activation functions from (a) the power transformation (Yeo-Johnson) layer and (b) the Lambert $W \times F_X$ layer.

3 Related work

End-to-end NNs for inverse problems There are vast amounts of end-to-end neural networks designed for inverse problems, using CNNs [9, 25, 59], GANs [46, 44, 65], invertible networks [2], and diffusion models [28]. The general idea is simple: train a neural network that directly maps observed data to estimated parameters. Even though such methods seem effective in a few applications, DGM-regularized inversion with our Gaussianization layers is preferable for the following reasons. First, the forward modeling can be so expensive computationally that it is infeasible to collect a decent training dataset for some applications. For example, one large-scale fluid mechanics or wave propagation simulation can take hours, if not days. Second, the relationship between parameters and data can be highly nonlinear, and multiple solutions may exist. An end-to-end network may map data to interpolated solutions that are not realistic. In comparison, our method can start from different initializations or even employ sampling techniques to address this issue. Third, the configuration of data collection can change from experiment to experiment. It is unbearable, for example, to re-train the network each time we change the number and locations of sensors. In contrast, not only can our method deal with this situation, but it can even use the same DGM for different forward models, as we can see in the compressive sensing MRI and eikonal tomography examples. Almost all end-to-end methods are only applied to linear inverse problems, whereas our Gaussianization layers are also effective in nonlinear problems.

Other techniques to improve DGM-regularized inversion In high-dimensional space, the probability mass of a standard Gaussian distribution concentrates within the so-called Gaussian typical set (Appendix G). To be in the Gaussian typical set, one necessary but not sufficient condition is to be within an annulus area around a high-dimensional sphere (Appendix G). Utilizing this geometric property, DGM-regularized inversion methods like [6] and [40] force updated latent vectors to stay on the sphere. This strategy is closely related to spherical interpolation [68]. We call this strategy the **spherical constraint** for inversion. In the original StyleGAN2 paper, the authors also noticed that in image projection tasks, the noise maps tend to have leakage from signals [27] – the same phenomenon we discussed. They proposed a multi-scale noise regularization term (**NoiseRlg**) to penalize spatial correlation in noise maps. We extend the same technique to our inverse problems for comparison. Note that we use a whitening layer before the ICA layer. The **whitening layer** can be used alone, similar to [20] and [57], whose performance will be reported in ablation studies. Also, [69] observed that for StyleGAN2, the Leaky ReLU function can “Gaussianize” latent vectors in the W space. **CSGM-w** [29] utilizes this *a priori* knowledge to improve DGM-regularized compressive sensing problems. Recently, score-based generative models have been shown to be promising for solving inverse problems [24, 58]. Currently, they seem only applicable to linear inverse problems. In addition, we propose an alternative idea to ensure latent vectors are within the standard Gaussian distribution. We reparameterize latent vectors using learnable orthogonal matrices (Cayley parameterization) and keep initial latent vectors fixed, which is closely related to the work of orthogonal over-parameterized training [42]. We refer readers to Appendix H for details on this technique.

4 Experiments

We consider three representative inversion problems for testing: compressive sensing MRI, image deblurring, and eikonal travelttime tomography. For MRI and eikonal tomography, we used synthetic brain images as inversion targets and used the pre-trained StyleGAN2 weights from [29] (trained on data from the databases of fastMRI [72, 34], TCIA-GBM [55], and OASIS-3 [35]) for regularization. We used the test split of the CelebA-HQ dataset [26] for deblurring, and the DGM is a Glow network trained on the training split. We refer readers to Appendix E for details on datasets and training.

We tested each parameter configuration in each inversion on 100 images (25 in the eikonal tomography due to its expensive forward modeling). Since the deep generative models are highly nonlinear, the results may get stuck in local minima. Thus, we started inversion using three different randomly initialized latent tensors for each of the 100 or 25 images, picked the best value among the three for each metric, and reported the mean and standard deviation of those metrics, except for CSGM-w and TV, where the initialization is fixed. The metrics we used were PSNR, SSIM [66], and an additional LPIPS [73] for the CelebA-HQ data. We used the LBFGS [50] optimizer in all experiments except TV, noise regularization, and CSGM-w, which use FISTA [4] or ADAM [30]. The temperature was set to 1.0 for StyleGAN2 and 0.7 for Glow.

4.1 Compressive sensing MRI using StyleGAN2

The mathematical model of compressive sensing MRI is

$$\mathbf{d} = \mathbf{A}\mathbf{m} + \epsilon, \quad (12)$$

where $\mathbf{A} \in \mathbb{C}^{M \times N}$ is the sensing matrix, which consists of FFT and subsampling in the k-space (frequency domain). Eq. 12 is an under-determined system, and we use $\text{Accl} = N/M$ to denote the acceleration ratio. We also added i.i.d. Gaussian noise with a signal-to-noise ratio (SNR) of 20 dB or 10 dB to the measured data. See Appendix A.1 for more background information.

Table 1 summarizes the comparison of results from total variation regularization (TV), noise regularization (NoiseRlg) [27], spherical constraint/reparameterization: $\mathbf{z} = \mathbf{v}/\|\mathbf{v}\|_2 * \sqrt{\dim(\mathbf{v})}$, CSGM-w [29], our proposed orthogonal reparameterization (Orthogonal), and our proposed Gaussianization layers (G layers). Fig. 5 shows examples of inversion results. In the base case where $\text{Accl}=8x$ and $\text{SNR}=20$ dB, the Gaussianization layers gives the best scores. Their advantage gets more significant when data SNR decreases to 10 dB. We also notice that scores from all methods are greatly improved if we make the system better determined (*i.e.*, $\text{Accl}=2x$). Also, the performance of TV, spherical constraint, and Gaussianization layers are similar in this scenario. We conclude that our proposed Gaussianization layers are effective and more robust than other methods.

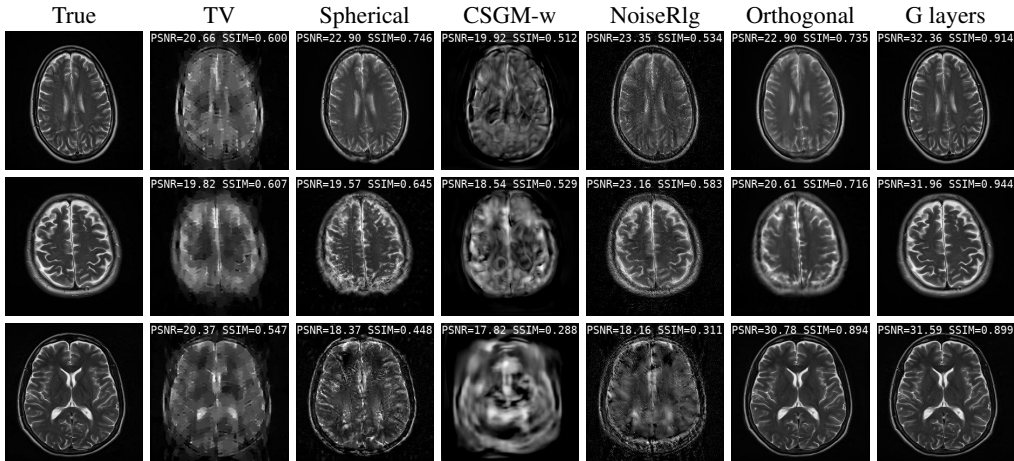


Figure 5: Comparison of compressive sensing MRI inversion results ($\text{Accl}=8x$, $\text{SNR}=20$ dB).

Table 1: Comparison of compressive sensing MRI results.

Method	Accl = 8x, SNR = 20 dB		Accl = 8x, SNR = 10 dB		Accl = 2x, SNR = 20 dB	
	PSNR \uparrow	SSIM \uparrow	PSNR \uparrow	SSIM \uparrow	PSNR \uparrow	SSIM \uparrow
TV	20.20 \pm 1.33	0.60 \pm 0.063	19.78 \pm 1.32	0.57 \pm 0.058	32.92 \pm 1.36	0.91 \pm 0.024
Spherical	26.93 \pm 6.57	0.79 \pm 0.159	22.78 \pm 5.38	0.61 \pm 0.246	32.90 \pm 3.50	0.90 \pm 0.061
CSGM-w	20.19 \pm 2.11	0.57 \pm 0.096	19.98 \pm 1.94	0.55 \pm 0.091	27.53 \pm 2.98	0.74 \pm 0.085
NoiseRgl	21.61 \pm 2.27	0.50 \pm 0.073	18.09 \pm 1.05	0.27 \pm 0.036	28.04 \pm 1.46	0.66 \pm 0.037
Orthogonal	26.14 \pm 5.79	0.78 \pm 0.134	25.10 \pm 5.08	0.77 \pm 0.132	29.29 \pm 5.32	0.84 \pm 0.108
G layers	27.99 \pm 5.70	0.83 \pm 0.128	25.48 \pm 4.76	0.78 \pm 0.149	32.41 \pm 4.60	0.90 \pm 0.079

Ablation study Table 2 summarizes the ablation study on the components of the Gaussianization layers. We kept the standardization layer on for all cases. The conclusions are as follows: 1. The ICA layer is the most significant part in improving result scores; 2. The whitening/ZCA layer is not effective; 3. The Yeo-Johnson (YJ) and the Lambert $W \times F_X$ (Lambt) layers are more effective when the noise level is higher (*e.g.*, $\text{SNR}=10$ dB vs. 20 dB). Their performance seems data-dependent: when $\text{SNR}=20$ dB, YJ seems more effective, while Lambt gives the best scores when $\text{SNR}=10$ dB. But the overall improvement from these two layers is marginal. In practice, one may only use ICA and one of the 1D Gaussianization layers. Additionally, we tested the effect of patch size on the \mathbf{z} (style) vectors (Appendix B). We find that the largest possible patch size gives the best results.

Table 2: Ablation study of the Gaussianization layers.

Method	Accl = 8x, SNR = 20 dB		Accl = 8x, SNR = 10 dB	
	PSNR↑	SSIM↑	PSNR↑	SSIM↑
ICA (✗), YJ (✗), Lambt (✗)	26.93±6.40	0.787±0.153	22.98±5.54	0.604±0.252
ICA (✗), YJ (✓), Lambt (✗)	26.92±6.42	0.787±0.156	23.14±5.44	0.622±0.245
ICA (✗), YJ (✗), Lambt (✓)	25.33±5.89	0.743±0.163	23.58±5.19	0.695±0.189
ZCA, YJ (✗), Lambt (✗)	27.08±6.52	0.786±0.157	22.94±5.50	0.623±0.235
ICA (✓), YJ (✗), Lambt (✗)	27.91±5.77	0.824±0.129	25.22±4.76	0.770±0.154
ICA (✓), YJ (✓), Lambt (✗)	27.99±5.70	0.831±0.128	25.48±4.76	0.779±0.149
ICA (✓), YJ (✗), Lambt (✓)	27.21±5.74	0.816±0.125	25.57±4.98	0.779±0.148
ICA (✓), YJ (✓), Lambt (✓)	27.37±5.90	0.819±0.135	25.09±4.91	0.771±0.144

4.2 Image deblurring using Glow

The mathematical model for deblurring is

$$\mathbf{d} = \mathbf{G} * \mathbf{m} + \epsilon, \quad (13)$$

where \mathbf{G} is a smoothing filter and $*$ denotes convolution. We used a Gaussian smoothing filter with a standard deviation of 3, and added noise $\epsilon \sim \mathcal{N}(\mathbf{0}, 50^2\mathbf{I})$ to the observed data. Although the system may not be under-determined, the high-frequency information is lost due to low-pass filtering; hence this is also an ill-posed problem. Though we only tested on facial images, deblurring has wide applications in astronomy and geophysics. See Appendix A.2 for more background information.



Figure 6: Comparison of deblurring results from different methods.

Table 3 and Fig. 6 show that the Gaussianization layers are also effective in Glow, better than using the spherical constraint or the orthogonal reparameterization. We also demonstrate the efficacy of Gaussianization layers when the forward model is inaccurate, in which case the induced error in data is not Gaussian (Appendix B).

Ablation study Table 3 also shows that the two parameterization schemes (Appendix C) for Glow using the Gaussianization layers have similar performance. Besides, we report the ablation study on components of the Gaussianization layers for Glow (Appendix B).

4.3 Eikonal tomography using StyleGAN2

In acoustic wave imaging (e.g., ultrasound tomography), we excite waves using sparsely distributed sources one at a time at the boundary of the object. Then we reconstruct its internal structures (the spatial distribution of wave speed) given the first-arrival travel time recorded on the boundary. The following eikonal equation approximately describes the shortest travel time $T(\mathbf{x}; \mathbf{x}_s)$ that the acoustic wave emerging from the source location \mathbf{x}_s takes to reach location \mathbf{x} inside the target object [71]:

$$|\nabla T(\mathbf{x}; \mathbf{x}_s)| = 1/c(\mathbf{x}), \quad T(\mathbf{x}_s; \mathbf{x}_s) = 0, \quad (14)$$

where $c(\mathbf{x})$ is the wave propagation speed at each location. Both this eikonal PDE and the implicitly defined forward mapping $c(\mathbf{x}) \rightarrow T(\mathbf{x})$ are nonlinear, and there has been little research on DGM-regularized inverse problems with such nonlinear characteristics. The inverse problem is severely ill-posed, which is equivalent to a curved-ray tomography problem. See Appendix A.3 for more

background information. We added noise to the recorded travel time using the following formula: $T_{\text{noisy}}(\mathbf{x}_r; \mathbf{x}_s) = T(\mathbf{x}_r; \mathbf{x}_s)(1 + \epsilon)$, where $\epsilon \sim \mathcal{N}(0, 0.001^2)$ and \mathbf{x}_r denotes any receiver location. In other words, longer traveltimes corresponds to larger uncertainties.

We show that Gaussianization layers outperformed other methods in this tomography task in Table 4 and Fig. 7. Note that this is a statistical conclusion. We also report an example where the spherical constraint works better than the Gaussianization layers (bottom right).

Table 3: Deblurring results using Glow.

Method	LPIPS↓	PSNR↑	SSIM↑
Spherical	0.17±0.06	21.78±1.14	0.580±0.066
Orthogonal	0.16±0.06	21.91±1.31	0.583±0.063
G layers P1	0.13±0.05	22.40±1.34	0.583±0.069
G layers P2	0.13±0.05	22.47±1.27	0.590±0.064

Table 4: Eikonal tomography using StyleGAN2

Method	PSNR↑	SSIM↑
TV	20.66±1.21	0.543±0.073
Spherical	22.19±4.05	0.686±0.144
G layers	24.46±3.58	0.775±0.144

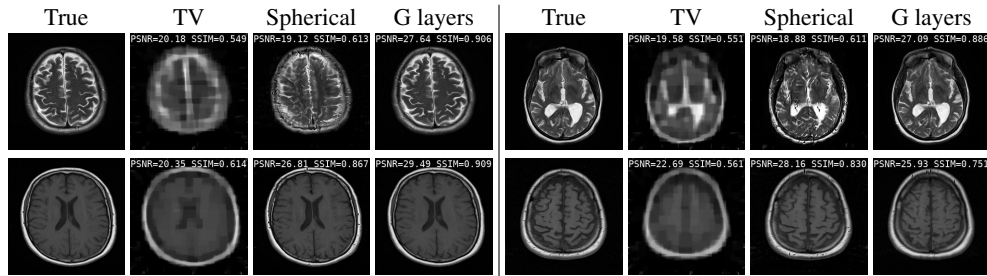


Figure 7: Comparison of eikonal tomography results from different methods.

5 Conclusions

We further discuss this work’s limitations, computational cost, and broader impact in Appendix I.

In summary, we have introduced a set of Gaussianization layers: the ICA layer (with a whitening layer), the power transformation layer, the Lambert $W \times F_X$ layer, and the standardization layer that are sequentially stacked together to reparameterize and Gaussianize latent vectors for inverse problems regularized by deep generative models. These layers approximately keep the latent vector traversing within the standard Gaussian distribution or typical set so that inversion results remain plausible. We have demonstrated the efficacy and advantages of our proposed layers on three representative inverse problems from computational imaging. The method is general and can be applied to various deep generative models, which we have proved using two state-of-the-art generators: StyleGAN2 and Glow.

A Background of forward models

A.1 Compressive sensing MRI

The MRI process essentially samples the spatial frequency components of a target, following some trajectories in the spatial frequency space (k-space) according to the design of the physical system. For example, a system may sample the k-space line-by-line horizontally/vertically or in radial directions. If the k-space has been fully sampled on a Cartesian grid, one can directly use inverse FFT to reconstruct the image. For various practical reasons, however, it is necessary to speed up the data collection process, usually by skipping data points in the k-space, which can be mathematically represented by a masking operation. In addition, there can be multiple coils with different sensitivity maps collecting data simultaneously. The mathematical formulation reads

$$\mathbf{d}_i = \mathbf{P}\mathbf{F}\mathbf{S}_i\mathbf{m} + \epsilon, \quad i = 1, \dots, N_{\text{coils}} \quad (15)$$

where $\mathbf{d}_i \in \mathbb{C}^N$ is the k-space data corresponding to the i -th coil, $\mathbf{m} \in \mathbb{R}^N$ is the target object, $\mathbf{P} \in \mathbb{R}^{N \times N}$ is the mask, $\mathbf{F} \in \mathbb{C}^{N \times N}$ is the Fourier transform operator, $\mathbf{S}_i \in \mathbb{R}^{N \times N}$ is the point-wise sensitivity map (a diagonal matrix) corresponding to the i -th coil, and ϵ denotes noise.

To ensure a fair comparison with prior work and reproducibility, we used the same masks from the repository of [29] (Fig. 8). In addition, we also used the same single-coil setup as in [29], where the sensitivity matrix is an identity matrix.

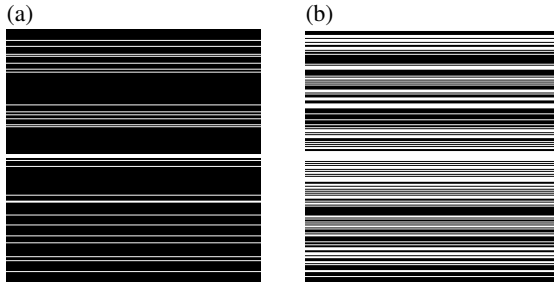


Figure 8: Masks for compressive sensing MRI [29]. White: 1, black: 0. (a) $8\times$ acceleration; (b) $2\times$ acceleration.

We condense the effects of all operators into a linear operator $\mathbf{A} \in \mathbb{C}^{M \times N}$ and arrive at the under-determined system

$$\mathbf{d} = \mathbf{A}\mathbf{m} + \epsilon \quad (12)$$

from the main text, where we use $\text{Accl} = N/M$ to denote the acceleration ratio.

A.2 Deblurring

The mathematical model behind deblurring is

$$\mathbf{d} = \mathbf{G} * \mathbf{m} + \epsilon, \quad (16)$$

where \mathbf{G} is a smoothing filter, $*$ denotes convolution, and ϵ is noise.

The purpose of deblurring is to recover the original sharp image \mathbf{m} given a noisy blurred observation \mathbf{d} . In this study, we showed deblurring examples for natural images. In scientific applications, deblurring or deconvolution is also a powerful tool. For example, in astronomy, \mathbf{d} is a blurred image from a telescope, \mathbf{G} is a point-spread function (PSF) constructed from the physics model of the telescope, and we want to obtain a sharper image from the observation [60]. In geophysics, \mathbf{d} can be the seismic data, \mathbf{G} is a calibrated wavelet, and we want to obtain sharp images of reflectivities defining the boundaries of subsurface strata [41, 74]. In general, \mathbf{G} is a low-pass or band-pass filter, so certain frequency contents are lost in the forward process. The deblurring or deconvolution process needs to recover such missing information. In addition, the noise makes the inversion process unstable. The deblurring or deconvolution problem is thus ill-posed.

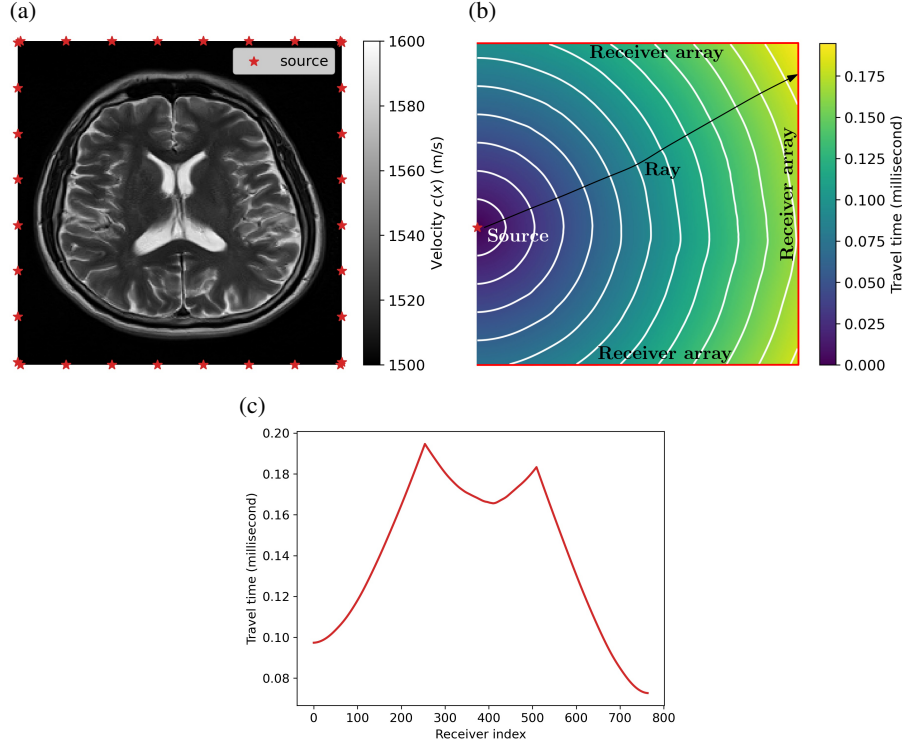


Figure 9: Experimental setup for eikonal tomography. (a) The target image and source locations; (b) Travel time field and the receiver array corresponding to the source. The contours are wavefronts. The propagation of waves can be viewed as curved rays traveling in directions perpendicular to such wavefronts; (c) The profile of the shortest wave travel time recorded at the receiver array. The receiver index starts from 0 in the top-right corner in subfigure (b) and increases in the clockwise direction.

A.3 Eikonal tomography

In acoustic wave imaging (e.g., ultrasound tomography), we excite waves using sparsely distributed sources one at a time at the boundary of the object. Then we reconstruct its internal structures (the spatial distribution of wave speed) given the first-arrival travel time recorded on the boundary. The following eikonal equation describes the shortest travel time $T(\mathbf{x}; \mathbf{x}_s)$ that the acoustic wave emerging from the source location \mathbf{x}_s takes to reach location \mathbf{x} inside the target object in the high-frequency limit [71]:

$$|\nabla T(\mathbf{x}; \mathbf{x}_s)| = 1/c(\mathbf{x}), \quad T(\mathbf{x}_s; \mathbf{x}_s) = 0, \quad (17)$$

where $c(\mathbf{x})$ is the wave propagation speed at each location. Both this eikonal PDE and the implicitly defined forward mapping $c(\mathbf{x}) \rightarrow T(\mathbf{x})$ are nonlinear.

To be more specific, we show the setup of our experiment in Fig. 9(a). For the convenience of numerical testing, we put sources and receivers on the boundaries of a square box that contains the object, suggesting that the object is immersed in a square box filled with water. In reality, one can put sources and receivers directly on the target. The dimension of the square area is $25.6 \text{ cm} \times 25.6 \text{ cm}$ with a grid interval of 0.001 m . There are eight sources located on each side, and receivers are located at each grid point on the boundary. Fig. 9(b) shows the shortest travel time field of the generated wave from the indicated source location. For each source, we only use receivers on the three other sides, indicated by the red lines, excluding the one on which the source is located. Fig. 9(c) shows the profile of the shortest wave travel time recorded at the receiver array. The receiver index starts from 0 in the top-right corner and increases in the clockwise direction.

We can interpret the nonlinearity and ill-posedness of eikonal tomography from another perspective. As shown in Fig. 9(b), we plot contours $T(\mathbf{x}) = \text{const}$ representing the wavefronts. Under the high-frequency approximation, the propagation of waves can be viewed as curved rays traveling in directions perpendicular to such wavefronts. Since the wavefronts depend on velocity field $c(\mathbf{x})$, the

rays are also functionals of the parameter $c(\boldsymbol{x})$ to be estimated, contrary to straight-ray tomography such as CT. The eikonal inversion problem is thus nonlinear. Besides, the rays carry information about the medium averaged along their paths. One property of curved-ray tomography is that the ray coverage is uneven inside the object. In fact, curved rays tend to avoid low-velocity areas, giving us little information about such regions, making the inverse problem intrinsically ill-posed.

We solved the eikonal equation using the fast sweeping method [75] and computed the gradient using the discrete adjoint-state method, using the code from the repository of [39].

Our eikonal tomography uses the same StyleGAN2 network as the compressive sensing MRI experiments. The value range of StyleGAN2 is $[-1, 1]$. In the forward model, we map the StyleGAN2 output to $c(\boldsymbol{x})$ in two steps. First, we convert it values to the range of $[0, 1]$ by using $\mathbf{m} \leftarrow (\mathbf{m} + 1)/2$. Second, we convert the values to the range of acoustic wave velocity using $\mathbf{m} \leftarrow 100 \times \mathbf{m} + 1500$. This relationship is purely manufactured for our synthetic tests. One should use a more realistic relationship in practice.

B Additional experiments

First, we report in Table 5 an ablation study on the effects of various combinations of regularization techniques on style vectors and noise maps in StyleGAN2. The observations are 1. If we turn off the update of noise maps, the Gaussianization layers lead to the best result; 2. If we turn on the update of noise maps, applying the Gaussianization layers to both the style vectors and noise maps gives the best results.

Table 5: Ablation study on different combinations of regularization on the style vectors and noise maps in StyleGAN2 for compressive sensing MRI. In the parentheses, “u” stands for unconstrained, “g” stands for reparameterization with the Gaussianization layers, “o” stands for orthogonal reparameterization, and “ \mathbf{X} ” means that the update is turned off.

Method	Accl = 8x, SNR = 20 dB		Accl = 8x, SNR = 10 dB	
	PSNR \uparrow	SSIM \uparrow	PSNR \uparrow	SSIM \uparrow
Style (u), Noise (\mathbf{X})	26.58 \pm 5.90	0.80 \pm 0.137	25.57 \pm 5.24	0.78 \pm 0.137
Style (g), Noise (\mathbf{X})	27.39 \pm 5.26	0.83 \pm 0.124	27.02 \pm 4.57	0.82 \pm 0.122
Style (o), Noise (\mathbf{X})	25.88 \pm 5.74	0.78 \pm 0.134	25.39 \pm 5.09	0.77 \pm 0.131
Style (u), Noise (u)	26.51 \pm 6.51	0.77 \pm 0.163	22.49 \pm 5.62	0.57 \pm 0.266
Style (g), Noise (o)	27.43 \pm 6.04	0.81 \pm 0.134	24.93 \pm 4.27	0.76 \pm 0.128
Style (o), Noise (o)	26.14 \pm 5.79	0.78 \pm 0.134	25.10 \pm 5.08	0.77 \pm 0.132
Style (o), Noise (g)	26.04 \pm 5.70	0.78 \pm 0.134	25.22 \pm 5.12	0.77 \pm 0.133
Style (g), Noise (g)	27.99 \pm 5.70	0.83 \pm 0.128	25.48 \pm 4.76	0.78 \pm 0.149

Second, we studied the effect of patch size on the performance of Gaussianization layers. To be more specific, we tested the effects of various patch sizes on 1D style vectors. The largest patch size is 64 since the number of extracted patches should not be smaller than the dimension of the patches. We only turned on the ICA layer and the standardization layer in this experiment. One can observe that both the PSNR and the SSIM increase as the patch size increases. We would advise using the largest possible patch size in Gaussianization layers, although we only used a patch size of 32 for style vectors in all other experiments.

In all experiments, we fixed the patch size for Glow as $3 \times 8 \times 8$ and the patch size for the noise maps in StyleGAN2 as $1 \times 8 \times 8$. In the experiments with Glow, the image dimension was $3 \times 128 \times 128$. If we chose a larger patch size, we could not obtain enough patch vectors. As for StyleGAN2, if we look at the parameterization illustrated in Fig. 10, there is already a 4×4 noise map unconstrained if we choose the patch size as 8×8 . If we increase the patch size to $1 \times 16 \times 16$, there will be two additional 8×8 noise maps unconstrained. To minimize the influence of unconstrained parameters, we chose the patch size for noise maps as $1 \times 8 \times 8$.

Third, we did a parameter sweep on the weighting parameter β in the Glow-regularized deblurring problem (formulation 3 or 43). Consistent with Fig. 1, the conventional Glow-based regularization is

Table 6: Ablation study on patch size of the style vectors in StyleGAN2.

Method	PSNR \uparrow	SSIM \uparrow
Patch size = 8	25.33 \pm 6.42	0.76 \pm 0.155
Patch size = 16	26.83 \pm 6.57	0.79 \pm 0.144
Patch size = 32	27.91 \pm 5.77	0.82 \pm 0.129
Patch size = 64	28.03 \pm 5.44	0.83 \pm 0.130

not as effective as our Gaussianization layers. If β is too large (e.g., 10 or 100), the inversion results become unrealistic with huge errors.

Table 7: Glow-regularized deblurring results using different β s.

Method	LPIPS \downarrow	PSNR \uparrow	SSIM \uparrow
$\beta = 0.0$	0.172 \pm 0.06	21.74 \pm 1.27	0.58 \pm 0.072
$\beta = 0.01$	0.172 \pm 0.06	21.75 \pm 1.15	0.58 \pm 0.067
$\beta = 0.1$	0.174 \pm 0.06	21.72 \pm 1.15	0.57 \pm 0.069
$\beta = 1.0$	0.174 \pm 0.06	21.95 \pm 1.21	0.59 \pm 0.067
$\beta = 10.0$	0.247 \pm 0.08	22.55 \pm 1.10	0.58 \pm 0.086
$\beta = 100.0$	0.602 \pm 0.15	12.56 \pm 2.63	0.12 \pm 0.101

Fourth, we investigated the performance of Gaussianization layers when the forward model is inaccurate (Table 8). Our Gaussianization layers still outperform the conventional Glow-regularized inversion.

Table 8: Glow-regularized deblurring with an inaccurate filter. The ground-truth standard deviation of the Gaussian filter is 3, which is used to generate the observed data, but we used 5 for inversion.

Method	LPIPS \downarrow	PSNR \uparrow	SSIM \uparrow
Conventional ($\beta = 1.0$)	0.21 \pm 0.06	17.72 \pm 1.41	0.49 \pm 0.059
G layers	0.17 \pm 0.06	18.70 \pm 1.40	0.50 \pm 0.060

Finally, we did an ablation study on the components of Gaussianization layers in Glow-regularized deblurring (Table 9). We adopted the second parameterization scheme (Appendix C). The observations are similar to those from Table 2: 1. The ICA layer is the most significant part in improving result scores, especially LPIPS – the score that matches human perception the best; 2. The whitening/ZCA layer is not effective when used alone; 3. There is no clear winner among combinations of 1D Gaussianization layers, and their difference in performance is marginal. So we picked the Lambert $W \times F_X$ layer, one of the best-performing options, in all other deblurring experiments as the 1D Gaussianization layer.

C Reparameterization schemes for StyleGAN2 and Glow

Fig. 10 illustrates the reparameterization scheme for StylgeGAN2 using the Gaussianization layers. The patch size for the style vectors and noise maps are 32 and $1 \times 8 \times 8$, respectively. Note that we transpose the latent tensors in Fig. 10 compared to the notations in corresponding equations and algorithms.

For Glow, we came up with two reparameterization schemes (Fig. 11). The first one (P1) reparameterizes patches from a latent tensor with the same dimension as the output image. Then a multi-scale squeezing operation maps the latent tensor into a list of tensors corresponding to different scales of Glow. Glow uses the list of tensors as the input. The second scheme (P2) reparameterizes patches extracted directly from tensors in the above list. The unfolding and squeezing operations are illustrated in Fig. 12. In the multi-scale architecture of Glow, the squeezing operation is applied recursively on half of the output tensor cut in the channel direction [14, 31].

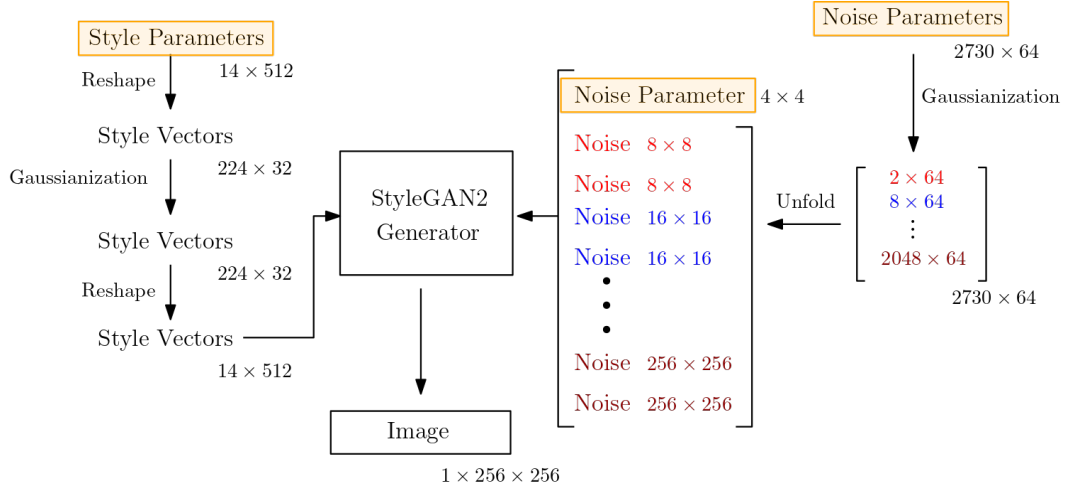


Figure 10: Reparameterization scheme for StyleGAN2. The dimensions of the latent parameters are [the number of vectors \times vector dimension], except the 4×4 one. Note that we transpose latent tensors in corresponding equations and algorithms.

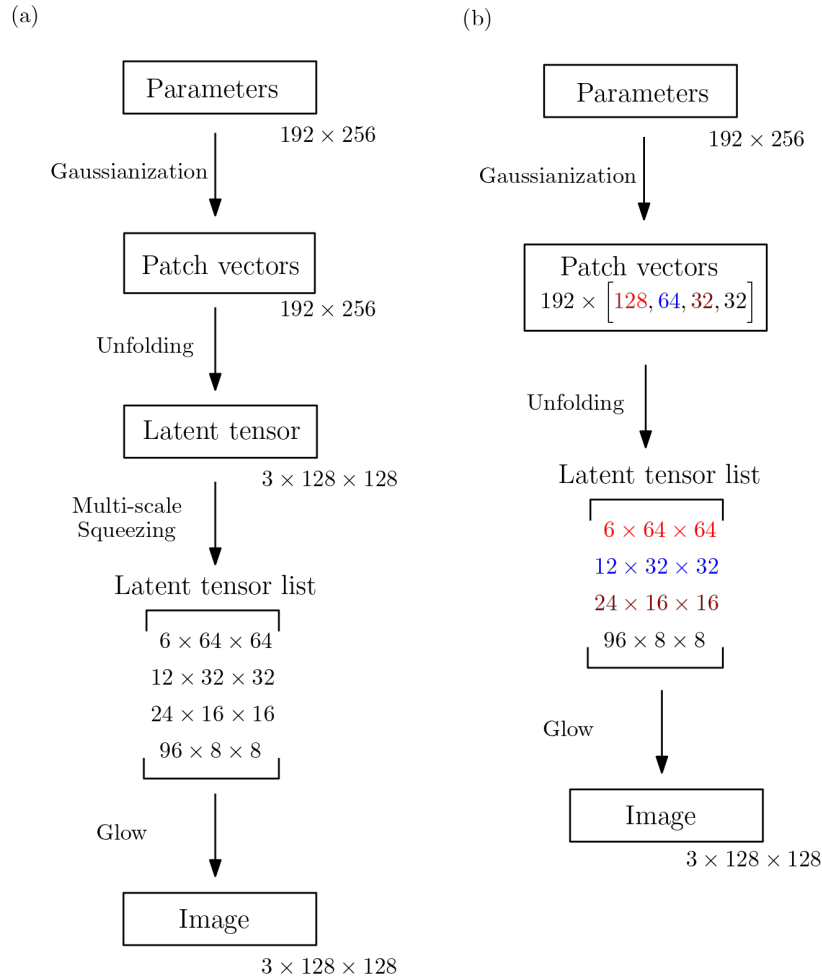


Figure 11: Two reparameterization schemes for Glow. (a) P1; (b) P2. The dimensions of the latent parameters are [vector dimension \times the number of vectors].

Table 9: Ablation study of the components of Gaussianization layers applied to Glow-regularized deblurring.

Method			LPIPS↓	PSNR↑	SSIM↑
ICA (✗),	YJ (✗),	Lambt (✗)	0.17±0.06	21.79±1.11	0.583±0.065
ICA (✗),	YJ (✗),	Lambt (✓)	0.16±0.06	21.96±1.31	0.588±0.065
ICA (✗),	YJ (✓),	Lambt (✗)	0.17±0.06	21.75±1.25	0.579±0.067
ICA (✗),	YJ (✓),	Lambt (✓)	0.16±0.06	21.99±1.20	0.587±0.066
ZCA,	YJ (✗),	Lambt (✗)	0.16±0.05	21.66±1.28	0.579±0.070
ICA (✓),	YJ (✗),	Lambt (✗)	0.14±0.06	22.52±1.30	0.586±0.070
ICA (✓),	YJ (✗),	Lambt (✓)	0.13±0.05	22.47±1.27	0.590±0.064
ICA (✓),	YJ (✓),	Lambt (✗)	0.14±0.05	22.49±1.35	0.586±0.070
ICA (✓),	YJ (✓),	Lambt (✓)	0.13±0.06	22.40±1.27	0.586±0.066

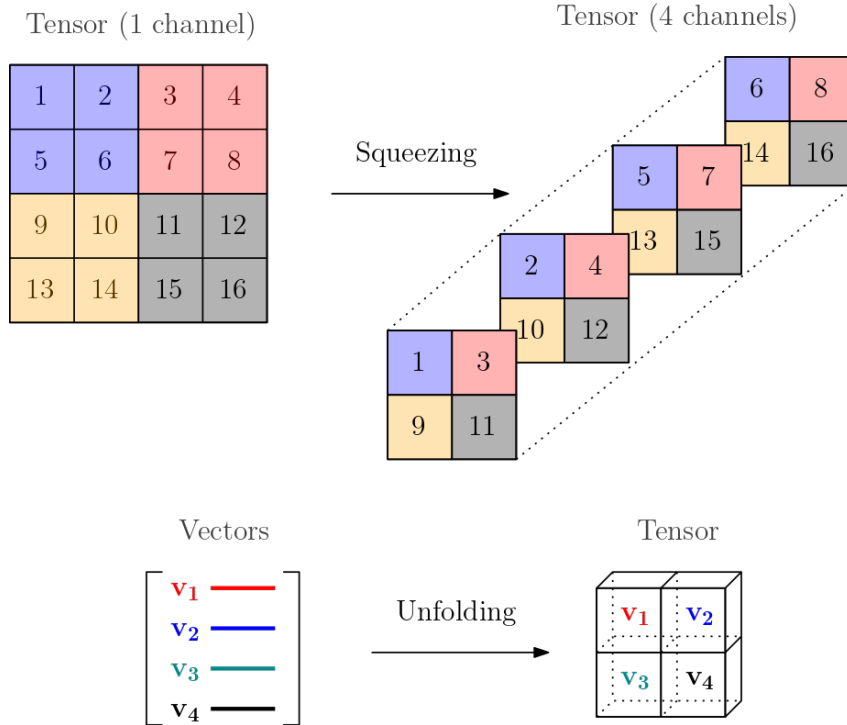


Figure 12: Illustration of the squeezing and unfolding operations.

D More details of the Gaussianization layers

D.1 ICA layer

The overall ICA layer is summarized in Algorithm 1. We set a maximum number of the fixed-point iterations to reduce computational cost and ensure accurate gradient computation that can pass the finite-difference convergence test. The gradients are backpropagated through the loops without using the trick introduced in Appendix F.

Whitening The FastICA algorithm typically requires that the data are pre-whitened. Let \mathbf{V} be the data matrix whose columns are data vectors. We first subtract the mean from the data vector using $\mathbf{V} \leftarrow \mathbf{V} - \text{mean}(\mathbf{V}, \text{dim} = 1)$. Then we compute the data covariance matrix using $\mathbf{C} = (1 - \eta) \frac{1}{N-1} \mathbf{V}\mathbf{V}^\top + \eta \mathbf{I}$, where we use a small constant (e.g., $\eta = 0.001$) to blend the empirical covariance matrix and an identity matrix to avoid ill-conditioning.

After these data preparation steps, the ZCA whitening used throughout the study first computes the eigenvalues $\mathbf{\Lambda}$ and eigenvectors \mathbf{D} , and then output the whitened data using $\mathbf{V} \leftarrow \mathbf{D}\mathbf{\Lambda}^{-1/2}\mathbf{D}^\top\mathbf{V}$.

Alternatively, we can use the following steps to whiten the data, which are also used later in ICA iterations to decorrelate column vectors in the orthogonal matrix [21]:

1. Initialize $\mathbf{W} \leftarrow \mathbf{I}$;
2. Compute

$$\mathbf{W} \leftarrow \mathbf{W} / \sqrt{\|\mathbf{W}^\top \mathbf{C} \mathbf{W}\|_2} \quad (18)$$

3. Repeat until convergence

$$\mathbf{W} \leftarrow \frac{3}{2} \mathbf{W} - \frac{1}{2} \mathbf{W} \mathbf{W}^\top \mathbf{C} \mathbf{W}, \quad (19)$$

4. Output $\mathbf{V} \leftarrow \mathbf{W}^\top \mathbf{V}$

Algorithm 1: ICA Layer

Input : Data matrix $\mathbf{V} \in \mathbb{R}^{D \times N}$; error tolerance ϵ ; damping parameters: $\eta = 10^{-4}$ and $\alpha = 0.8$; maximum iteration numbers $J = 10$ and $K = 100$.

Output : Matrix $\mathbf{P} \in \mathbb{R}^{D \times N}$ with i.i.d. entries

// Whitening stage

```

1  $\mathbf{V} = \mathbf{V} - \text{mean}(\mathbf{V}, \text{dim} = 1)$ ,  $\mathbf{C} = (1 - \eta) \frac{1}{N-1} \mathbf{V}\mathbf{V}^\top + \eta \mathbf{I}$ ;
2  $\mathbf{V} \leftarrow \text{ZCA-whitening}(\mathbf{V})$ ;
// ICA stage
3  $\mathbf{W} = \mathbf{W}^* \leftarrow \mathbf{I}$ ,  $j \leftarrow 1$ ;
4 while  $j \leq J$  do
5    $\mathbf{W} \leftarrow \frac{1}{N} \left[ \alpha \mathbf{V} \phi(\mathbf{W}^\top \mathbf{V})^\top - \mathbf{W} \text{diag}(\phi'(\mathbf{W}^\top \mathbf{V}) \mathbf{1}) \right]$  Eq. (7);
6    $\mathbf{W} = \mathbf{W}_0 \leftarrow \mathbf{W} / \sqrt{\|\mathbf{W}^\top \mathbf{W}\|_2}$ ,  $k \leftarrow 1$ ;
7   while  $k < K$  do
8      $\mathbf{W} \leftarrow \frac{3}{2} \mathbf{W} - \frac{1}{2} \mathbf{W} \mathbf{W}^\top \mathbf{W}$ ;
9     if  $\|\mathbf{W} - \mathbf{W}_0\| < \epsilon$  then
10       $\perp$  break;
11      $\mathbf{W}_0 \leftarrow \mathbf{W}$ ,  $k \leftarrow k + 1$ ;
12   if  $\|\mathbf{W} - \mathbf{W}^*\| < \epsilon$  then
13      $\perp$  break;
14    $\mathbf{W}^* \leftarrow \mathbf{W}$ ,  $j \leftarrow j + 1$ ;
15 return  $\mathbf{P} \leftarrow \mathbf{W}^\top \mathbf{V}$ .
```

The modified FastICA iterations. As stated in [22], the objective function for one neural unit of the weight vector \mathbf{w}_i and input \mathbf{v} is

$$\arg \max_{\mathbf{w}_i} \mathbb{E} [\Phi (\mathbf{w}_i^\top \mathbf{v})], \text{ s.t., } \mathbb{E} [(\mathbf{w}_i^\top \mathbf{v})^2] = 1, \quad (20)$$

where Φ is the contrast function (*e.g.*, logcosh). The original derivations convert this constrained optimization to an unconstrained one using Lagrange multipliers. However, this procedure is unnecessary since the matrix \mathbf{W} is orthogonalized after each iteration, and the input vectors have been pre-whitened. Therefore, we only need to solve the following equation

$$\mathbb{E}[\mathbf{v}\phi(\mathbf{w}_i^\top \mathbf{v})] = 0, \quad (21)$$

whose Jacobian is

$$\begin{aligned} J &= \mathbb{E}[\mathbf{v}\mathbf{v}^\top \phi'(\mathbf{w}_i^\top \mathbf{v})] \\ &\approx \mathbb{E}[\mathbf{v}\mathbf{v}^\top] \mathbb{E}[\phi'(\mathbf{w}_i^\top \mathbf{v})] = \mathbb{E}[\phi'(\mathbf{w}_i^\top \mathbf{v})], \end{aligned} \quad (22)$$

where ϕ is the derivative of Φ . The Newton iteration scheme is thus

$$\mathbf{w}_i = \mathbf{w}_i - \mathbb{E}[\mathbf{v}\phi(\mathbf{w}_i^\top \mathbf{v})] / \mathbb{E}[\phi'(\mathbf{w}_i^\top \mathbf{v})]. \quad (23)$$

To improve the convergence, we damp the iterations by a parameter $\alpha \in (0, 1)$. Also, using the same technique to convert the Newton iterations to fixed-point iterations in [22, 21], we arrive at the modified fixed-point iteration scheme:

$$\mathbf{w}_i = \alpha \mathbb{E}[\mathbf{v}\phi(\mathbf{w}_i^\top \mathbf{v})] - \mathbb{E}[\phi'(\mathbf{w}_i^\top \mathbf{v})] \mathbf{w}_i, \quad (24)$$

followed by the aforementioned decorrelation procedure after each step. The convergence of the modified FastICA iterations can be proved similarly as in [51].

D.2 Power transformation layer

Algorithm 2: Power Transformation Layer

Input : Data vector \mathbf{p}

Output : Vector \mathbf{s} whose values are 1D Gaussianized.

- 1 Estimate λ from \mathbf{p} using Eq. 9 ;
 - 2 Compute \mathbf{s} with the estimated λ and data \mathbf{p} using Eq. 8 ;
 - 3 **return** \mathbf{s} .
-

We use a custom operator based on SciPy’s implementation using Brent’s algorithm [8] to find an approximate minimum of Problem 9. Continuing from the approximate minimum, we use Brent’s root finding algorithm [8] to find the minimum where the gradient vanishes. Since the parameter λ depends on input data, we need to back-propagate the gradient through the optimization process.

The power transformation layer is summarized in Algorithm 2.

D.3 Lambert $W \times F_X$ layer

The transformation Eq. 10 is bijective if $\delta \geq 0$, and we can use the Lambert W function to find its inverse. The Lambert W function W is defined as the inverse of $q = W^{-1}(t) = t \exp(t)$, where t and q are scalars. Given q , Halley’s method can be used to find $t = W(q)$ [11]. Hence, the inverse of Eq. 10 is

$$X = W_\delta \left(\frac{S - \mu_X}{\sigma_X} \right) \sigma_X + \mu_X, \quad (25)$$

where

$$W_\delta(u) = \text{sign}(u) \sqrt{\frac{W(\delta u^2)}{\delta}}. \quad (26)$$

We use the parameterized Lambert $W \times F_X$ distribution family to approximate a heavy-tailed input distribution and use Eq. 25 to recover a distribution with lighter tails. In order to make the recovered

distribution close to a Gaussian distribution, we compute the optimal heavy-tail parameter δ by minimizing the difference between the kurtosis of the output distribution and 3 (Kurtosis is a common surrogate measure of negentropy [23]):

$$\hat{\delta}_{\text{GMM}} = \arg \min_{\delta > 0} \left| \text{Kurt} \left(W_{\delta} \left(\frac{\mathbf{s} - \mu_X}{\sigma_X} \right) \right) - 3 \right|^2, \quad (27)$$

where \mathbf{s} is the data vector, and Kurt is the kurtosis. We constrain $\delta > 0$, and solve Eq. 27 using the L-BFGS-B optimizer [76].

In addition, we estimate the mean μ_X and standard deviation σ_X along with δ using the Iterative Generalized Method of Moments (IGMM) [16], which embeds an optimization problem for δ in an outer loop of iterations to estimate σ_X and μ_X (see Algorithm 3). If the kurtosis of input data vector is not greater than 3, we skip the whole Lambert $W \times F_X$ layer by directly outputting the data vector.

Algorithm 3: Lambert $W \times F_X$ Layer with the Iterative Generalized Method of Moments (IGMM) [16]

Input : Data vector \mathbf{s} , error tolerance $\epsilon = 10^{-5}$, maximum iteration number $K = 100$.

Output : vector \mathbf{x} whose empirical distribution is less heavy-tailed than \mathbf{s} , and its kurtosis ≈ 3)

- 1 Initialize: $\xi^{(0)} \leftarrow (\hat{\mu}_X^{(0)}, \hat{\sigma}_X^{(0)}, \hat{\delta}^{(0)})$, $k = 0$;
 - 2 Compute initial kurtosis $\beta_2 = \text{Kurt}(\mathbf{s})$;
 - 3 **if** $\beta_2 \leq 3$ **then**
 - 4 | return \mathbf{s} ;
 - 5 **end**
 - 6 **while** $k < K$ and $\|\xi^{(k)} - \xi^{(k-1)}\| \geq \epsilon$ **do**
 - 7 | $\mathbf{u}^{(k)} \leftarrow (\mathbf{s} - \mu_X^{(k)}) / \sigma_X^{(k)}$;
 - 8 | Compute $\delta^{(k+1)}$ using Eq. 27; $\mathbf{u}^{(k+1)} \leftarrow \mathbf{W}_{\delta^{(k+1)}}(\mathbf{u}^{(k)})$; $\mathbf{x}^{(k+1)} \leftarrow \mathbf{u}^{(k+1)} \sigma_X^{(k)} + \mu_X^{(k)}$;
 - 9 | Update $\mu_X^{(k+1)} \leftarrow \mathbb{E}[\mathbf{x}^{(k+1)}]$, and $\sigma_X^{(k+1)} \leftarrow \sqrt{\text{Var}(\mathbf{x}^{(k+1)})}$;
 - 10 | $\xi^{(k+1)} \leftarrow (\hat{\mu}_X^{(k+1)}, \hat{\sigma}_X^{(k+1)}, \hat{\delta}^{(k+1)})$;
 - 11 | $k \leftarrow k + 1$;
 - 12 **end**
 - 13 **return** $\mathbf{x} = W_{\delta} \left(\frac{\mathbf{s} - \mu_X}{\sigma_X} \right) \sigma_X + \mu_X$,
-

E Details of datasets and training

For MRI and eikonal tomography, we generate synthetic brain images as inversion targets using the pre-trained StyleGAN2 weights from [29], which are trained on data from the databases of fastMRI [72, 34], TCIA-GBM [55], and OASIS-3 [35]. As a result, there is no sensitive personal information in our target images. In the data generation process, we only used one style vector of a dimension of 512. We picked 100 images that are visually plausible, whose random seeds can be found in our code. These random seeds were never used to initialize inversion. In inversion experiments, we used 14 such style parameters: one for the lowest resolution of 4×4 , one for the tRGB layer, and two for each resolution from 8×8 to 256×256 , to avoid inversion crime. This choice of expanding latent space dimension is also justified by our observation that only one style parameter vector is generally insufficient for inversion tasks with data from datasets such as CelebA-HQ [26].

We used the CelebA-HQ dataset [26] (under the Creative Commons CC BY-NC 4.0 license) for the deblurring experiments. All images were downsampled to the resolution of 128×128 . We split the 30000 images from CelebA-HQ into the subsets of training (24183 images), validation (2993 images), and testing (2824 images) following the original splits from CelebA [43]. For the inversion tests, we randomly selected 100 images from the test set.

For the hyper-parameters of the Glow networks, we used 4 multi-scale levels and 32 flow-steps, and we only used additive coupling layers. Fig. 13 reports the training process. For each epoch,

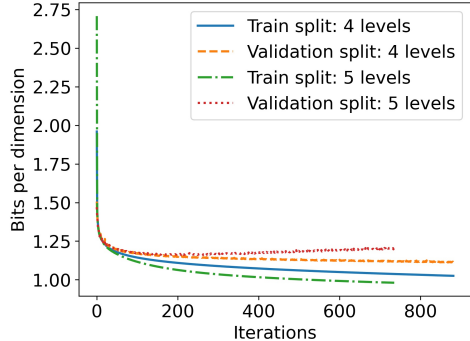


Figure 13: The negative log-likelihood or NLL (reported in bits per dimension) on the training and validation splits of the CelebA-HQ dataset with different numbers of multi-scale levels.

we computed the training negative log-likelihood (NLL) averaged throughout the epoch, and the validation NLL at the end of the epoch. The validation curves suggest that it is better to use 4 multi-scale levels. We chose the network weights from the epoch before the validation NLL stopped to decrease: 850 for the CelebA-HQ dataset. All training was conducted using 8×32 GB Nvidia V100 GPUs with a batch size of 64. We used the Adam optimizer [30] with a learning rate of 10^{-4} , as well as $\beta_1 = 0.9$ and $\beta_2 = 0.99$.

F Gradient computation of the optimization-based differentiable layers

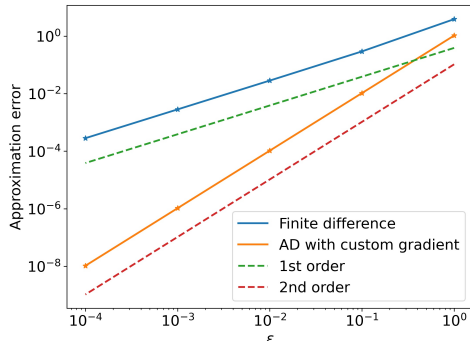


Figure 14: Gradient accuracy test for custom operators. An accurate gradient should make the error converge at a speed of the second order following the red dashed line.

In the power transformation and Lambert $W \times F_X$ layers, there are operators whose outputs are obtained by solving optimization problems formally described as

$$\mathbf{y} = \arg \min_{\mathbf{y}} l(\mathbf{x}, \mathbf{y}), \quad (28)$$

where l denotes the objective function that defines the operator, symbol \mathbf{y} stands for the output, a scalar in our cases but can also be a vector in general situations. The optimal condition is

$$l_{\mathbf{y}}(\mathbf{x}, \mathbf{y}) := L(\mathbf{x}, \mathbf{y}) = 0, \quad (29)$$

where the subscript denotes partial differentiation.

The optimal condition implicitly defines a forward operator of the following form:

$$\mathbf{y} = \text{op}_{\text{forward}}(\mathbf{x}). \quad (30)$$

The backward operator is

$$\frac{\partial \chi}{\partial \mathbf{x}} = \text{op}_{\text{backward}}\left(\frac{\partial \chi}{\partial \mathbf{y}}, \mathbf{y}, \mathbf{x}\right), \quad (31)$$

where χ is the objective function of an inverse problem.

Differentiating Eq. 29 with respect to \mathbf{x} , we have

$$L_x + L_y \mathbf{y}_x = 0 \implies \mathbf{y}_x = -L_y^{-1} L_x, \quad (32)$$

using the implicit function theorem. Then, to back-propagate the gradient from $\frac{\partial \chi}{\partial \mathbf{y}}$ to $\frac{\partial \chi}{\partial \mathbf{x}}$, we use

$$\frac{\partial \chi}{\partial \mathbf{x}} = \frac{\partial \chi}{\partial \mathbf{y}} \mathbf{y}_x = -\frac{\partial \chi}{\partial \mathbf{y}} L_y^{-1} L_x = -\frac{\partial \chi}{\partial \mathbf{y}} H_y^{-1} L_x, \quad (33)$$

where H_y is the Hessian matrix of χ with respect to \mathbf{y} .

In our problems, the output \mathbf{y} is a scalar, so it is easy to use automatic differentiation to compute L_y directly and hence L_y^{-1} . Otherwise, if \mathbf{y} has many parameters, we can first solve the following linear system with an auxiliary vector $\boldsymbol{\lambda}$:

$$\boldsymbol{\lambda} H_y = -\frac{\partial \chi}{\partial \mathbf{y}}, \quad (34)$$

and then compute the gradient using

$$\frac{\partial \chi}{\partial \mathbf{x}} = \boldsymbol{\lambda} L_x, \quad (35)$$

a technique also known as the adjoint-state method. Note that there is no need to compute the Hessian explicitly, but one can use automatic differentiation to compute the vector-Hessian product $\boldsymbol{\lambda} H_y$ and utilize iterative linear solvers like GMRES [54] to solve the linear system.

As a final note, we check the accuracy of our gradient computation using the finite-difference convergence test based on Taylor expansion:

$$f(\mathbf{x} + \epsilon \delta \mathbf{x}) = f(\mathbf{x}) + \epsilon \nabla f(\mathbf{x})^\top \delta \mathbf{x} + \mathcal{O}(\epsilon^2), \quad (36)$$

where $\delta \mathbf{x}$ is a random vector with a unit ℓ_2 norm, and $\nabla f(\mathbf{x})$ is computed using our custom gradient. We here define f as a composite function that maps the (vector) output of an forward operator to a scalar, e.g., $f(\mathbf{x}) = \|\text{op}_{\text{forward}}(\mathbf{x})\|_2^2$. Once we decrease ϵ , we should see that the error term $f(\mathbf{x} + \epsilon \delta \mathbf{x}) - f(\mathbf{x}) - \epsilon \nabla f(\mathbf{x})^\top \delta \mathbf{x}$ decreases at a speed of the second order. All our layers passed this test, as the example shown in Fig. 14. This test should be conducted in double precision.

G Gaussian typical set

Theorem 1 (Gaussian Annulus Theorem [5]) *For a n -dimensional standard Gaussian, for any $\beta \leq \sqrt{n}$, all but at most $3e^{-c\beta^2}$ of the probability mass lies within the annulus $\sqrt{n} - \beta \leq |x| \leq \sqrt{n} + \beta$, where c is a fixed positive constant.*

Bojanowski *et al.* [6] recognized this issue in their generative latent optimization processes and projected the latent vector onto a sphere. In addition to constraining the norm of latent vectors only, our approach Gaussianizes the latent vectors. In fact, a latent vector staying within the Gaussian annulus geometrically does not necessarily map to a plausible image. For example, all latent vectors in Fig. 4 have almost the same ℓ_2 norm, but the leftmost one does not correspond to a meaningful normalizing flow output.

The formal definition of a typical set is as follows.

Definition 1 (Cover & Thomas [12]) *Let $p_X(x)$ be a distribution whose support is \mathcal{X} . The typical set $A_\epsilon^{(n)}$ is defined as the set of sequences $(x_1, x_2, \dots, x_n) \in \mathcal{X}^n$, $x_i \stackrel{i.i.d.}{\sim} p_X$ that satisfy*

$$\left| H[X] + \frac{1}{n} \log p_X(x_1, \dots, x_n) \right| \leq \epsilon, \quad (37)$$

where $H[X]$ is the entropy of random variable X .

Now a random vector $\mathbf{x} \in \mathbb{R}^n \sim \mathcal{N}(\mathbf{0}, \sigma^2 \mathbf{I})$ can be factorized as i.i.d. random variables that are distributed as $\mathcal{N}(0, \sigma^2)$. Therefore, we can regard \mathbf{x} as an i.i.d. sequence and give the following definition:

Definition 2 (Gaussian Typical Set) A Gaussian typical set is the typical set $A_\epsilon^{(n)}$ of $\mathbf{x} \in \mathbb{R}^n \sim \mathcal{N}(\mathbf{0}, \sigma^2 \mathbf{I})$.

The following theorem guarantees that a typical sample from $\mathbf{x} \in \mathbb{R}^n \sim \mathcal{N}(\mathbf{0}, \sigma^2 \mathbf{I})$ resides in the Gaussian typical set with very high probability.

Theorem 2 (Cover & Thomas [12]) For every $\epsilon > 0$, the typical set has probability $P(A_\epsilon^{(n)}) > 1 - \epsilon$ with a sufficiently large dimension n .

These theoretical facts again justify our Gaussianization approach, which first makes each component as independent as possible and then shapes each component towards the same marginal 1D Gaussian distribution. As a result, the Gaussianization layers shape a latent vector towards a typical example from the desired high-dimensional isotropic Gaussian distribution.

H Orthogonal reparameterization

We also propose to reparameterize the latent vector \mathbf{z} using an orthogonal matrix \mathbf{R} :

$$\mathbf{z} = \mathbf{R}\mathbf{v}, \mathbf{v} \sim \mathcal{N}(\mathbf{0}, \mathbf{I}), \quad (38)$$

where \mathbf{v} is fixed during an inversion, and we treat \mathbf{R} as the parameter instead. There are various ways to parameterized an orthogonal matrix. We choose the Cayley parameterization:

$$\mathbf{R} = (\mathbf{I} + \mathbf{W})(\mathbf{I} - \mathbf{W})^{-1}, \text{ where } \mathbf{W} = -\mathbf{W}^\top, \quad (39)$$

one of the best reported in [42]. Therefore, the DGM-regularized inversion using orthogonal reparameterization is

$$\arg \min_{\mathbf{W}} (1/2) \|\mathbf{d} - f \circ g(\mathbf{R}\mathbf{v})\|_2^2. \quad (40)$$

The specific reparameterization schemes for StyleGAN2 and Glow are the same as in Appendix C. For style vectors, we use the full dimension of 512 because of the observation described in Table 6. For Glow and noise maps in StyleGAN2, we use patch sizes $3 \times 8 \times 8$ and $1 \times 8 \times 8$, respectively, to save computation time and memory.

I Additional discussions

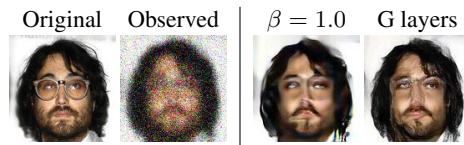


Figure 15: A failure example where inversion is unable to restore the eyeglasses because of the strong constraint from traversing within the Gaussian typical set. The results are dominated by the bias of the training dataset.

We point out the limitations of this work. First, requiring latent vectors to traverse within the Gaussian distribution/typical set means that the statistics of the training dataset will dominate the results. Fig. 15 shows that our method cannot restore the eyeglasses because it is not a significant feature within our training data. One needs to pay particular attention to training dataset construction to ensure that it represents the typical features to be investigated. One should also interpret their results with this caveat in mind. Second, we make the i.i.d. assumption about latent patches, which may not be valid since neighboring pixels from different patches may not be independent. Still, our method works well in practice, and we also have designed the rolling operation (Appendix J.3) that shifts the patch extraction locations to improve performance if necessary. Third, since the deep generative models are highly nonlinear, the results may get stuck in local minima. We mitigate this problem by starting inversion from multiple randomly initialized latent vectors. However, this technique is computationally expensive. It is an important research direction to improve the initialization process.

The Gaussianization layers are based on optimization and fixed-point iterations, which can be computationally expensive. With one V100 GPU and an Intel Xeon Platinum 8276 CPU, it takes around 1.95 ± 0.30 seconds and 1.18 ± 0.21 seconds to finish one forward computation and one custom gradient back-propagation, respectively. The computation time was estimated by 1000 repeated experiments. Nevertheless, the additional computation time is acceptable if the physics simulation takes a much longer time.

We use 100 V100 GPUs to run experiments in parallel. Our rough estimation is that all experiments can be finished within one week with these resources.

We believe that this study can benefit both the broader scientific community and the general public. However, we point out that the MRI and eikonal tomography experiments are purely synthetic and numerical. They do not fully reflect realistic medical imaging configurations. One should be cautious about applying our techniques to real data and interpreting the results.

J Miscellaneous topics

J.1 Inversion using Glow

In the Glow-regularization framework, we solve the inverse problem by finding the maximum *a posteriori* (MAP) estimate from

$$p_M(\mathbf{m}|\mathbf{d}) \propto p(\mathbf{d}|\mathbf{m}) p_M(\mathbf{m}), \quad (41)$$

where M denotes the parameter space. The probability density p_M introduces our *a priori* knowledge and is represented by a normalizing flow (Glow) g_θ , which is a differentiable invertible mapping between two distributions, parameterized by neural network parameters θ : $\mathbf{m} = g_\theta(\mathbf{z})$, where \mathbf{z} is the latent vector. After training, the log probability density of a given model \mathbf{m} is

$$\log p_M(\mathbf{m}; \theta) = \log p_Z(g_\theta^{-1}(\mathbf{m})) + \log \left| \det J_{g_\theta^{-1}}(\mathbf{m}) \right| = \log p_Z(\mathbf{z}) - \log \left| \det J_{g_\theta}(\mathbf{z}) \right|, \quad (42)$$

where Z stands for the latent space. When we use the trained network in inversion, we freeze the network weights; hence, we drop θ in g_θ hereafter in our notation. Therefore, Eq. 3 for Glow-regularized inversion is

$$\arg \min_{\mathbf{z}} (1/2) \|\mathbf{d} - f \circ g(\mathbf{z})\|_2^2 - \beta (\log p_Z(\mathbf{z}) - \log \left| \det J_g(\mathbf{z}) \right|). \quad (43)$$

The new regularization term in Eq. 3 is $\mathcal{R}'(\mathbf{z}) = -\beta (\log p_Z(\mathbf{z}) - \log \left| \det J_g(\mathbf{z}) \right|)$, and we have shown the results with different β s in Fig. 1 and Table 7.

J.2 Duality of KL divergence

As also shown in [53], the KL-divergence between two distributions does not change under a differentiable invertible transformation, so

$$D_{\text{KL}} [p_M^*(\mathbf{m}) \| p_M(\mathbf{m}; \theta)] = D_{\text{KL}} [p_Z^*(\mathbf{z}; \theta) \| p_Z(\mathbf{z})], \quad (44)$$

where p_M^* is the target distribution in the physical parameter space, and p_Z^* is the corresponding latent-space distribution under the normalizing flow. This means that minimizing the forward KL divergence in the M domain or physical parameter space is equivalent to minimizing the reverse KL-divergence in the Z domain or the latent space.

This fact and Theorem 2 imply that a well-trained normalizing flow maps samples from the target distribution into the Gaussian typical set with very high probability and vice versa.

J.3 The rolling operation

After applying one set of the Gaussianization layers to the latent tensor, it might be desirable to apply the layers to a different set of non-overlapping patches from the latent tensor again. The rolling operation shifts the latent tensor in the horizontal and vertical directions by half of the patch size w before patch extractions. The values at the boundaries are wrapped around to the opposite sides. One can, for example, use the `torch.roll` command to implement this functionality.

References

- [1] Kazunori Akiyama, Antxon Alberdi, Walter Alef, Keiichi Asada, Rebecca Azulay, Anne-Kathrin Baczko, David Ball, Mislav Baloković, John Barrett, Dan Bintley, et al. First m87 event horizon telescope results. iv. imaging the central supermassive black hole. *The Astrophysical Journal Letters*, 875(1):L4, 2019.
- [2] Lynton Ardizzone, Jakob Kruse, Sebastian Wirkert, Daniel Rahner, Eric W Pellegrini, Ralf S Klessen, Lena Maier-Hein, Carsten Rother, and Ullrich Köthe. Analyzing inverse problems with invertible neural networks. *arXiv preprint arXiv:1808.04730*, 2018.
- [3] Muhammad Asim, Max Daniels, Oscar Leong, Ali Ahmed, and Paul Hand. Invertible generative models for inverse problems: mitigating representation error and dataset bias. In *International Conference on Machine Learning*, pages 399–409. PMLR, 2020.
- [4] Amir Beck and Marc Teboulle. A fast iterative shrinkage-thresholding algorithm for linear inverse problems. *SIAM journal on imaging sciences*, 2(1):183–202, 2009.
- [5] Avrim Blum, John Hopcroft, and Ravindran Kannan. *Foundations of data science*. Cambridge University Press, 2020.
- [6] Piotr Bojanowski, Armand Joulin, David Lopez-Paz, and Arthur Szlam. Optimizing the latent space of generative networks. *arXiv preprint arXiv:1707.05776*, 2017.
- [7] Ashish Bora, Ajil Jalal, Eric Price, and Alexandros G Dimakis. Compressed sensing using generative models. In *International Conference on Machine Learning*, pages 537–546. PMLR, 2017.
- [8] Richard P Brent. *Algorithms for minimization without derivatives*. Courier Corporation, 2013.
- [9] Hu Chen, Yi Zhang, Mannudeep K Kalra, Feng Lin, Yang Chen, Peixi Liao, Jiliu Zhou, and Ge Wang. Low-dose ct with a residual encoder-decoder convolutional neural network. *IEEE transactions on medical imaging*, 36(12):2524–2535, 2017.
- [10] Scott Chen and Ramesh Gopinath. Gaussianization. *Advances in neural information processing systems*, 13:423–429, 2000.
- [11] Robert M Corless, Gaston H Gonnet, David EG Hare, David J Jeffrey, and Donald E Knuth. On the lambertw function. *Advances in Computational mathematics*, 5(1):329–359, 1996.
- [12] Thomas M Cover and Joy A Thomas. *Elements of Information Theory*. Wiley, 2012.
- [13] Laurent Dinh, David Krueger, and Yoshua Bengio. Nice: Non-linear independent components estimation. *arXiv preprint arXiv:1410.8516*, 2014.
- [14] Laurent Dinh, Jascha Sohl-Dickstein, and Samy Bengio. Density estimation using real nvp. *arXiv preprint arXiv:1605.08803*, 2016.
- [15] H Gemmeke and NV Ruiters. 3d ultrasound computer tomography for medical imaging. *Nuclear Instruments and Methods in Physics Research Section A: Accelerators, Spectrometers, Detectors and Associated Equipment*, 580(2):1057–1065, 2007.
- [16] Georg M Goerg. The lambert way to gaussianize heavy-tailed data with the inverse of tukey’sh transformation as a special case. *The Scientific World Journal*, 2015, 2015.
- [17] Ian J Goodfellow, Jean Pouget-Abadie, Mehdi Mirza, Bing Xu, David Warde-Farley, Sherjil Ozair, Aaron Courville, and Yoshua Bengio. Generative adversarial networks. *arXiv preprint arXiv:1406.2661*, 2014.
- [18] Paul Hand, Oscar Leong, and Vladislav Voroninski. Phase retrieval under a generative prior. *arXiv preprint arXiv:1807.04261*, 2018.
- [19] JA Högbom. Aperture synthesis with a non-regular distribution of interferometer baselines. *Astronomy and Astrophysics Supplement Series*, 15:417, 1974.
- [20] Lei Huang, Dawei Yang, Bo Lang, and Jia Deng. Decorrelated batch normalization. In *Proceedings of the IEEE Conference on Computer Vision and Pattern Recognition*, pages 791–800, 2018.
- [21] Aapo Hyvarinen. Fast and robust fixed-point algorithms for independent component analysis. *IEEE transactions on Neural Networks*, 10(3):626–634, 1999.

- [22] Aapo Hyvärinen. The fixed-point algorithm and maximum likelihood estimation for independent component analysis. *Neural Processing Letters*, 10(1):1–5, 1999.
- [23] Aapo Hyvärinen and Erkki Oja. Independent component analysis: algorithms and applications. *Neural networks*, 13(4-5):411–430, 2000.
- [24] Ajil Jalal, Marius Arvinte, Giannis Daras, Eric Price, Alexandros G Dimakis, and Jon Tamir. Robust compressed sensing mri with deep generative priors. *Advances in Neural Information Processing Systems*, 34:14938–14954, 2021.
- [25] Kyong Hwan Jin, Michael T McCann, Emmanuel Froustey, and Michael Unser. Deep convolutional neural network for inverse problems in imaging. *IEEE Transactions on Image Processing*, 26(9):4509–4522, 2017.
- [26] Tero Karras, Timo Aila, Samuli Laine, and Jaakko Lehtinen. Progressive growing of gans for improved quality, stability, and variation. In *ICLR*, 2018.
- [27] Tero Karras, Samuli Laine, Miika Aittala, Janne Hellsten, Jaakko Lehtinen, and Timo Aila. Analyzing and improving the image quality of stylegan. In *Proceedings of the IEEE/CVF conference on computer vision and pattern recognition*, pages 8110–8119, 2020.
- [28] Bahjat Kawar, Michael Elad, Stefano Ermon, and Jiaming Song. Denoising diffusion restoration models. *arXiv preprint arXiv:2201.11793*, 2022.
- [29] Varun A Kelkar and Mark Anastasio. Prior image-constrained reconstruction using style-based generative models. In *International Conference on Machine Learning*, pages 5367–5377. PMLR, 2021.
- [30] Diederik Kingma and Jimmy Ba. Adam, a method for stochastic optimization. In *ICLR*, 2015.
- [31] Diederik P Kingma and Prafulla Dhariwal. Glow: Generative flow with invertible 1x1 convolutions. *arXiv preprint arXiv:1807.03039*, 2018.
- [32] Diederik P Kingma, Tim Salimans, Rafal Jozefowicz, Xi Chen, Ilya Sutskever, and Max Welling. Improving variational inference with inverse autoregressive flow. *arXiv preprint arXiv:1606.04934*, 2016.
- [33] Diederik P Kingma and Max Welling. Auto-encoding variational bayes. *arXiv preprint arXiv:1312.6114*, 2013.
- [34] Florian Knoll, Jure Zbontar, Anuroop Sriram, Matthew J Muckley, Mary Bruno, Aaron Defazio, Marc Parente, Krzysztof J Geras, Joe Katsnelson, Hersh Chandarana, et al. fastmri: A publicly available raw k-space and dicom dataset of knee images for accelerated mr image reconstruction using machine learning. *Radiology: Artificial Intelligence*, 2(1):e190007, 2020.
- [35] Pamela J LaMontagne, Tammie LS Benzinger, John C Morris, Sarah Keefe, Russ Hornbeck, Chengjie Xiong, Elizabeth Grant, Jason Hassenstab, Krista Moulder, Andrei G Vlassenko, et al. Oasis-3: longitudinal neuroimaging, clinical, and cognitive dataset for normal aging and alzheimer disease. *MedRxiv*, 2019.
- [36] Valero Laparra, Gustavo Camps-Valls, and Jesús Malo. Iterative gaussianization: from ica to random rotations. *IEEE transactions on neural networks*, 22(4):537–549, 2011.
- [37] Paul C Lauterbur. Image formation by induced local interactions: examples employing nuclear magnetic resonance. *nature*, 242(5394):190–191, 1973.
- [38] Dongzhuo Li, Huseyin Denli, Cody MacDonald, Kyle Basler-Reeder, Anatoly Baumstein, and Jacquelyn Daves. Multiparameter geophysical reservoir characterization augmented by generative networks. In *First International Meeting for Applied Geoscience & Energy*, pages 1364–1368. Society of Exploration Geophysicists, 2021.
- [39] Dongzhuo Li, Kailai Xu, Jerry M Harris, and Eric Darve. Coupled time-lapse full-waveform inversion for subsurface flow problems using intrusive automatic differentiation. *Water Resources Research*, 56(8):e2019WR027032, 2020.
- [40] Jingyun Liang, Kai Zhang, Shuhang Gu, Luc Van Gool, and Radu Timofte. Flow-based kernel prior with application to blind super-resolution. In *Proceedings of the IEEE/CVF Conference on Computer Vision and Pattern Recognition*, pages 10601–10610, 2021.
- [41] LR Lines and S Treitel. A review of least-squares inversion and its application to geophysical problems. *Geophysical prospecting*, 32(2):159–186, 1984.

- [42] Weiyang Liu, Rongmei Lin, Zhen Liu, James M Rehg, Liam Paull, Li Xiong, Le Song, and Adrian Weller. Orthogonal over-parameterized training. In *Proceedings of the IEEE/CVF Conference on Computer Vision and Pattern Recognition*, pages 7251–7260, 2021.
- [43] Ziwei Liu, Ping Luo, Xiaogang Wang, and Xiaoou Tang. Deep learning face attributes in the wild. In *Proceedings of International Conference on Computer Vision (ICCV)*, December 2015.
- [44] Andreas Lugmayr, Martin Danelljan, Luc Van Gool, and Radu Timofte. Srflow: Learning the super-resolution space with normalizing flow. In *European Conference on Computer Vision*, pages 715–732. Springer, 2020.
- [45] Michael Lustig, David Donoho, and John M Pauly. Sparse mri: The application of compressed sensing for rapid mr imaging. *Magnetic Resonance in Medicine: An Official Journal of the International Society for Magnetic Resonance in Medicine*, 58(6):1182–1195, 2007.
- [46] Morteza Mardani, Enhao Gong, Joseph Y Cheng, Shreyas S Vasawala, Greg Zaharchuk, Lei Xing, and John M Pauly. Deep generative adversarial neural networks for compressive sensing mri. *IEEE transactions on medical imaging*, 38(1):167–179, 2018.
- [47] Razvan V Marinescu, Daniel Moyer, and Polina Golland. Bayesian image reconstruction using deep generative models. *arXiv preprint arXiv:2012.04567*, 2020.
- [48] Lukas Mosser, Olivier Dubrulle, and Martin J Blunt. Stochastic seismic waveform inversion using generative adversarial networks as a geological prior. *Mathematical Geosciences*, 52(1):53–79, 2020.
- [49] Andrew Ng. Independent components analysis. *CS229 Lecture notes*, 2000.
- [50] Jorge Nocedal and Stephen Wright. *Numerical optimization*. Springer Science & Business Media, 2006.
- [51] Erkki Oja and Zhijian Yuan. The fastica algorithm revisited: Convergence analysis. *IEEE transactions on Neural Networks*, 17(6):1370–1381, 2006.
- [52] Gregory Ongie, Ajil Jalal, Christopher A Metzler, Richard G Baraniuk, Alexandros G Dimakis, and Rebecca Willett. Deep learning techniques for inverse problems in imaging. *IEEE Journal on Selected Areas in Information Theory*, 1(1):39–56, 2020.
- [53] George Papamakarios, Theo Pavlakou, and Iain Murray. Masked autoregressive flow for density estimation. *arXiv preprint arXiv:1705.07057*, 2017.
- [54] Youcef Saad and Martin H Schultz. Gmres: A generalized minimal residual algorithm for solving nonsymmetric linear systems. *SIAM Journal on scientific and statistical computing*, 7(3):856–869, 1986.
- [55] Lisa Scarpace, L Mikkelsen, T Cha, Sujaya Rao, Sangeeta Tekchandani, S Gutman, and D Pierce. Radiology data from the cancer genome atlas glioblastoma multiforme [tcga-gbm] collection. *The Cancer Imaging Archive*, 11(4):1, 2016.
- [56] Ali Siahkoobi, Gabrio Rizzuti, Mathias Louboutin, Philipp A Witte, and Felix J Herrmann. Preconditioned training of normalizing flows for variational inference in inverse problems. *arXiv preprint arXiv:2101.03709*, 2021.
- [57] Aliaksandr Siarohin, Enver Sangineto, and Nicu Sebe. Whitening and coloring batch transform for gans. In *International Conference on Learning Representations*, 2018.
- [58] Yang Song, Liyue Shen, Lei Xing, and Stefano Ermon. Solving inverse problems in medical imaging with score-based generative models. *arXiv preprint arXiv:2111.08005*, 2021.
- [59] Anuroop Sriram, Jure Zbontar, Tullie Murrell, Aaron Defazio, C Lawrence Zitnick, Nafissa Yakubova, Florian Knoll, and Patricia Johnson. End-to-end variational networks for accelerated mri reconstruction. In *International Conference on Medical Image Computing and Computer-Assisted Intervention*, pages 64–73. Springer, 2020.
- [60] Jean-Luc Starck, Eric Pantin, and Fionn Murtagh. Deconvolution in astronomy: A review. *Publications of the Astronomical Society of the Pacific*, 114(800):1051, 2002.
- [61] Albert Tarantola. Inversion of seismic reflection data in the acoustic approximation. *Geophysics*, 49(8):1259–1266, 1984.
- [62] Jeroen Tromp, Carl Tape, and Qinya Liu. Seismic tomography, adjoint methods, time reversal and banana-doughnut kernels. *Geophysical Journal International*, 160(1):195–216, 2005.

- [63] Dave Van Veen, Ajil Jalal, Mahdi Soltanolkotabi, Eric Price, Sriram Vishwanath, and Alexandros G Dimakis. Compressed sensing with deep image prior and learned regularization. *arXiv preprint arXiv:1806.06438*, 2018.
- [64] Jean Virieux and Stéphane Operto. An overview of full-waveform inversion in exploration geophysics. *Geophysics*, 74(6):WCC1–WCC26, 2009.
- [65] Xintao Wang, Ke Yu, Shixiang Wu, Jinjin Gu, Yihao Liu, Chao Dong, Yu Qiao, and Chen Change Loy. Esrgan: Enhanced super-resolution generative adversarial networks. In *Proceedings of the European conference on computer vision (ECCV) workshops*, pages 0–0, 2018.
- [66] Zhou Wang, Alan C Bovik, Hamid R Sheikh, and Eero P Simoncelli. Image quality assessment: from error visibility to structural similarity. *IEEE transactions on image processing*, 13(4):600–612, 2004.
- [67] Jay Whang, Qi Lei, and Alex Dimakis. Solving inverse problems with a flow-based noise model. In *Proceedings of the 38th International Conference on Machine Learning*, volume 139 of *Proceedings of Machine Learning Research*, pages 11146–11157. PMLR, 18–24 Jul 2021.
- [68] Tom White. Sampling generative networks. *arXiv preprint arXiv:1609.04468*, 2016.
- [69] Jonas Wulff and Antonio Torralba. Improving inversion and generation diversity in stylegan using a gaussianized latent space. *arXiv preprint arXiv:2009.06529*, 2020.
- [70] In-Kwon Yeo and Richard A Johnson. A new family of power transformations to improve normality or symmetry. *Biometrika*, 87(4):954–959, 2000.
- [71] Özdoğan Yilmaz. *Seismic data analysis*, volume 1. Society of exploration geophysicists Tulsa, 2001.
- [72] Jure Zbontar, Florian Knoll, Anuroop Sriram, Tullie Murrell, Zhengnan Huang, Matthew J Muckley, Aaron Defazio, Ruben Stern, Patricia Johnson, Mary Bruno, et al. fastmri: An open dataset and benchmarks for accelerated mri. *arXiv preprint arXiv:1811.08839*, 2018.
- [73] Richard Zhang, Phillip Isola, Alexei A Efros, Eli Shechtman, and Oliver Wang. The unreasonable effectiveness of deep features as a perceptual metric. In *CVPR*, 2018.
- [74] Rui Zhang and John Castagna. Seismic sparse-layer reflectivity inversion using basis pursuit decomposition. *Geophysics*, 76(6):R147–R158, 2011.
- [75] Hongkai Zhao. A fast sweeping method for eikonal equations. *Mathematics of computation*, 74(250):603–627, 2005.
- [76] Ciyou Zhu, Richard H Byrd, Peihuang Lu, and Jorge Nocedal. Algorithm 778: L-bfgs-b: Fortran subroutines for large-scale bound-constrained optimization. *ACM Transactions on mathematical software (TOMS)*, 23(4):550–560, 1997.